



# U-Pb Dating on Hydrothermal Rutile and Monazite from the Badu Gold Deposit Supports an Early Cretaceous Age for Carlin-Type Gold Mineralization in the Youjiang Basin, Southwestern China

Wei Gao,<sup>1</sup> Ruizhong Hu,<sup>1,2,†</sup> Albert H. Hofstra,<sup>3</sup> Qiuli Li,<sup>4</sup> Jingjing Zhu,<sup>1</sup> Keqiang Peng,<sup>1</sup> Lan Mu,<sup>1,2</sup> Yong Huang,<sup>1</sup> Jianwen Ma,<sup>5</sup> and Qiang Zhao<sup>5</sup>

<sup>1</sup>*State Key Laboratory of Ore Deposit Geochemistry, Institute of Geochemistry, Chinese Academy of Sciences, Guiyang 550081, China*

<sup>2</sup>*College of Earth and Planetary Sciences, University of Chinese Academy of Sciences, Beijing 100049, China*

<sup>3</sup>*U.S. Geological Survey, Mail Stop 963, Box 25046, Denver, Colorado 80225, USA*

<sup>4</sup>*State Key Laboratory of Lithospheric Evolution, Institute of Geology and Geophysics, Chinese Academy of Sciences, Beijing 100029, China*

<sup>5</sup>*Jinfeng Mining Company, Tianlin 533315, China*

## Abstract

The Youjiang basin on the southwestern margin of the Yangtze block in southwestern China is the world's second largest Carlin-type gold province after Nevada, USA. The lack of precise age determinations on gold deposits in this province has hindered understanding of their genesis and relation to the geodynamic setting. Although most Carlin-type gold deposits in the basin are hosted in calcareous sedimentary rocks, ~70% of the ore in the Badu Carlin-type gold deposit is hosted by altered and sulfidized dolerite. Although in most respects Badu is similar to other Carlin-type gold deposits in the province, alteration of the unusual dolerite host produced hydrothermal rutile and monazite that can be dated.

Field observations show that gold mineralization is spatially associated with, but temporally later than, dolerite. In situ secondary ion mass spectrometry (SIMS) U-Pb dating on magmatic zircon from the least altered dolerite yielded a robust emplacement age of  $212.2 \pm 1.9$  Ma ( $2\sigma$ , mean square of weighted deviates [MSWD] = 0.55), providing a maximum age constraint on gold mineralization. The U-Th/He ages of detrital zircons from hydrothermally mineralized sedimentary host rocks at Badu and four other Carlin-type gold deposits yielded consistent weighted mean ages of 146 to 130 Ma that record cooling from a temperature over 180° to 200°C and place a lower limit on the age of gold mineralization in the basin.

Hydrothermal rutile and monazite that are coeval with gold mineralization have been identified in the mineralized dolerite. Rutile is closely associated with hydrothermal ankerite, sericite, and gold-bearing pyrite. It has high concentrations of W, Fe, V, Cr, and Nb, as well as growth zones that are variably enriched in W, Fe, Nb, and U. Monazite contains primary two-phase fluid inclusions and is intergrown with gold-bearing pyrite and hydrothermal minerals. In situ SIMS U-Pb dating of rutile yielded a Tera-Wasserburg lower intercept age of  $141.7 \pm 5.8$  Ma ( $2\sigma$ , MSWD = 1.04) that is within error of the in situ SIMS Th-Pb age of  $143.5 \pm 1.4$  Ma ( $2\sigma$ , MSWD = 1.5) on monazite. These ages are ~70 m.y. younger than magmatic zircons in the host dolerite and are similar to the aforementioned U-Th/He cooling ages on detrital zircons from hydrothermally mineralized sedimentary host rocks. We, therefore, conclude that the Badu Carlin-type gold deposit formed at ca. 144 Ma. The agreement of the rutile and monazite ages with the U-Th/He cooling ages of Badu and four other Carlin-type gold deposits in the Youjiang basin suggests that ca. 144 Ma is representative of a regional Early Cretaceous Carlin-type hydrothermal event formed during back-arc extension.

## Introduction

Carlin-type gold deposits in Nevada, USA, and the Youjiang basin, southwestern China, are some of the most important producers of gold in the world (Hu et al., 2002, 2017; Cline et al., 2005; Cline, 2018; Su et al., 2018). These deposits are primarily hosted in carbonate-bearing sedimentary rocks and characterized by carbonate dissolution, silicification, sulfidation, and argillic alteration (Hu et al., 2002, 2017; Hofstra and Cline, 2000; Cline et al., 2005; Cline, 2018; Kesler et al., 2005). Gold occurs mainly as invisible forms of structurally bounded Au<sup>1+</sup> and/or nanoparticles in arsenian pyrite (Simon et al., 1999; Palenik et al., 2004; Reich et al., 2005; Su et al., 2008, 2012). In whole rocks, Au is associated with anomalous

concentrations of As, Sb, Hg, and Tl, as well as high Au/Ag ratios (Cline et al., 2005; Hu et al., 2017). Nevada and the Youjiang basin are endowed with approximately 7,000 and 800 tons (t) of gold, respectively, making them the most important metallogenic provinces for Carlin-type gold deposit in the world (Hu et al., 2017; Muntean and Cline, 2018).

Resolving mineralization age and its relationship to geodynamics is a fundamental step in understanding the ore genesis (e.g., Rasmussen et al., 2006). However, this constraint is particularly difficult to achieve for Carlin-type gold deposits, stemming partly from the fine-grained nature of the ore and gangue minerals and partly from the lack of minerals clearly related to gold mineralization that are amenable to radiometric dating (Hu et al., 2002, 2017; Arehart et al., 2003). In Nevada, the timing of Carlin-type gold mineralization had been

<sup>†</sup>Corresponding author: e-mail, huruizhong@vip.gyig.ac.cn

well constrained in a narrow range of ~42 to 36 Ma by precise U-Pb and Ar-Ar dates on pre- and post-ore dikes and Rb-Sr and Ar-Ar dates on hydrothermal galkhaite and adularia, which are clearly associated with gold formation (Hofstra et al., 1999; Tretbar et al., 2000; Arehart et al., 2003; Cline et al., 2005). This range reveals that the Carlin-type gold deposits in Nevada formed during the transition from contraction to extension resulting from rollback of the Farallon plate and provides evidence for the close relationship between gold mineralization and magmatism (Hofstra et al., 1999; Cline et al., 2005; Ressel and Henry, 2006; Muntean et al., 2011). Unfortunately, igneous dikes are rare and galkhaite and adularia have not been reported from Carlin-type gold deposits in the Youjiang basin. Significant efforts have been expended in attempts to date Carlin-type gold deposits in the Youjiang basin, and the best constraints are from bulk analyses of mineral separates, such as those from calcite Sm-Nd, sulfide Re-Os, and sericite Ar-Ar dating (Su et al., 2009b; Wang, 2013; Chen et al., 2009a, 2015; Pi et al., 2016; Dong, 2017; Jin, 2017). Most of these dates, however, are of questionable reliability because of the broad range of ages obtained, their large errors, multiple stages of sulfides and sericite, low Re and Os contents of sulfides, and equivocal relationships between the dated minerals and gold formation. In situ dating on hydrothermal rutile and apatite also yielded significantly different ages of 214 and 142 Ma, respectively (Pi et al., 2017; Chen et al., 2019). Thus, there is no consensus on the age of Carlin-type gold deposits in the Youjiang basin, which has made it difficult to relate gold mineralization to specific geologic events and processes.

In Nevada, low-temperature thermochronology was also utilized to constrain the age of Carlin-type mineralization when other minerals clearly associated with gold formation were lacking (Arehart et al., 1993, 2003; Hofstra et al., 1999; Chakurian et al., 2003). However, zircon and apatite fission track systems have closure temperatures of 230° to 270°C and 90° to 120°C, respectively (Brandon et al., 1998; Ketcham et al., 1999; Reiners, 2005), which are higher and much lower than ore-forming temperatures of 180° to 240°C for Carlin-type gold deposits (Hu et al., 2002; Cline et al., 2005; Su et al., 2009a). Thus, these systems generally yielded a wide range of older or younger ages than that of Carlin-type gold mineralization in Nevada (Hofstra et al., 1999; Chakurian et al., 2003). In contrast, the zircon U-Th/He system has a closure temperature of 180° to 200°C (Reiners, 2005), which is low enough to be completely reset by hydrothermal activity associated with Carlin-type gold mineralization but high enough to decrease the possibility that the recorded ages are erased by postmineralization thermal events. Zircon U-Th/He data, therefore, can retain, or at least provide a lower limit on, the mineralization age.

Hydrothermal rutile and monazite are two common accessory minerals in many hydrothermal gold deposits that are highly resistant to weathering and post-ore modifications. Their low to high U and Th contents in the lattice (Li et al., 2003, 2011, 2013a, b; Schandl and Gorton, 2004; Meinhold, 2010) and high blocking temperatures for Pb diffusion (rutile, >500°C, Mezger et al., 1989; Vry and Baker, 2006; monazite, >700°C, Parrish, 1990) make them well suited for dating ore deposits. Advancements in analytical techniques and methods (e.g., secondary ion mass spectrometry [SIMS]; Li et al.,

2011, 2013a, b) now allow for in situ U-Th-Pb dating of rutile and monazite with a high spatial resolution and low detection limits.

Hydrothermal rutile commonly forms from the replacement of primary Ti-rich minerals in igneous host rocks (e.g., biotite, titanite, ilmenite, Ti magnetite; Rabbia et al., 2009; Pochon et al., 2017; Agangi et al., 2019). Because TiO<sub>2</sub>, the major oxide constituent of rutile, has extremely low solubility in hydrothermal fluids (Ayers and Watson, 1993; Meinhold, 2010), the whole-rock TiO<sub>2</sub> content and Ti-bearing minerals in the host rock are two key factors controlling rutile formation. Hydrothermal alteration of mafic rocks containing Ti-bearing ferromagnesian silicates and Fe-Ti oxides is more likely to generate hydrothermal rutile (Rabbia et al., 2009). Actually, for some Carlin-type, orogenic, and other hydrothermal gold deposits worldwide, which are uniquely hosted by felsic and/or mafic dikes, the primary Ti-rich minerals have been altered to hydrothermal rutile by ore-forming fluids associated with gold mineralization (Ressel et al., 2000; Emsbo et al., 2003; Velásquez et al., 2014; Doyle et al., 2015; Agangi et al., 2019; Pereira et al., 2019). Monazite is also a ubiquitous altered mineral and paragenetically associated with ore minerals in these deposits, and it has been widely used to constrain mineralization ages (Rasmussen et al., 2006; Sarma et al., 2008, 2011; Vielreicher et al., 2010, 2015; Fielding et al., 2017; Zhou et al., 2019).

In the southern part of the Youjiang basin, several gold deposits are also hosted in altered dolerite dikes, such as Badu, Shijia, Zhesang, and Anna, that are enriched in TiO<sub>2</sub> ranging from 2.4 to 4.3 wt % (Dong, 2017; Gao, 2018; Su et al., 2018). Among these deposits, Badu is the largest one. Despite their increasing economic importance, the dolerite-hosted deposits have been less studied than their counterparts hosted in sedimentary rocks. Knowledge on the mineralization and alteration characteristics of these dolerite-hosted deposits is valuable for deep understanding of low-temperature gold mineralization in the Youjiang basin. Importantly, if we can confidently identify hydrothermal rutile and monazite and conclusively establish their spatial and temporal textural associations with gold mineralization based on petrographic and geochemical signatures, they can provide robust geochronological clocks for in situ dating of Carlin-type gold mineralization in the Youjiang basin.

In this contribution, we present the results of comprehensive geologic, geochemical, and mineralogical investigations on the Badu gold deposit. The evidence gathered shows that Badu has alteration characteristics and mineral paragenesis that are similar to those of other sedimentary rock-hosted Carlin-type gold deposits (e.g., Jimfeng, Linwang, Jinya, and Nakuang) in the basin. In this context, Badu provides an excellent opportunity to apply hydrothermal rutile and monazite U-Pb dating to constrain the age of gold mineralization in the basin. To place a younger limit on the age of gold mineralization, zircon U-Th/He dating was applied to Badu and the other aforementioned sediment-hosted Carlin-type gold deposits. We also present textural and compositional characteristics of these deposits to place the analyzed samples in context. The combination of techniques applied provide compelling evidence that Carlin-type gold deposits in the Youjiang basin were produced by an Early Cretaceous hydrothermal event.

## Regional Geology

South China consists of the Yangtze and Cathaysia blocks, which were amalgamated along the Jiangshao suture zone in the early Neoproterozoic (Fig. 1a; Zhao et al., 2011). Subsequently, South China was affected by multiple orogenic events (Wang et al., 2013). Among these, the Triassic Indosinian orogeny is the most important, which resulted from collision between South China and North China to the north, and South China and Indochina block to the south, forming the Qinling-Dabie orogenic belt and the Song Ma suture zone, respectively (Hu et al., 2017).

The Youjiang basin, situated on the southwestern margin of the Yangtze block, is a diamond-shaped sedimentary basin controlled by a series of NE- and NW-striking basement-penetrating faults. It is separated from the Indochina block by the Red River-Ailaoshan fold belt to the southwest and from the Cathaysia block by the Pingxiang-Nanning fault to the southeast and is bounded by the Ziyun-Yadu fault and Mile-Shizong fault in the northeast and northwest, respectively (Fig. 1b;

Hu and Zhou, 2012; Hu et al., 2017). Tectonically, the basin is located at the transitional area between the Tethyan and Pacific tectonic domains (Chen et al., 2007). The basin lies on folded basement of lower Paleozoic strata and evolved in three stages: (1) rifting and development of passive continental margin sedimentation along the southwestern margin of the Precambrian Yangtze block due to opening of the Paleo-Tethys in Early Devonian to early Permian time (Du et al., 2009, 2013), (2) formation of a back-arc basin due to subduction of the Paleo-Tethys oceanic crust beneath South China during the late Permian (Du et al., 2009, 2013) or subduction of the Paleo-Pacific plate beneath the Eurasian plate during the middle Permian while the trench was more than 600 km from the basin (Li and Li, 2007), and (3) development of a foreland basin due to progressive closure of the Paleo-Tethys ocean basin and subsequent collision between the South China and Indochina block along the Song Ma suture to the south during the Middle-Late Triassic (Yan et al., 2006; Cai and Zhang, 2009; Yang et al., 2012; Qiu et al., 2016). Early to Middle Triassic sediments in the basin record the transi-

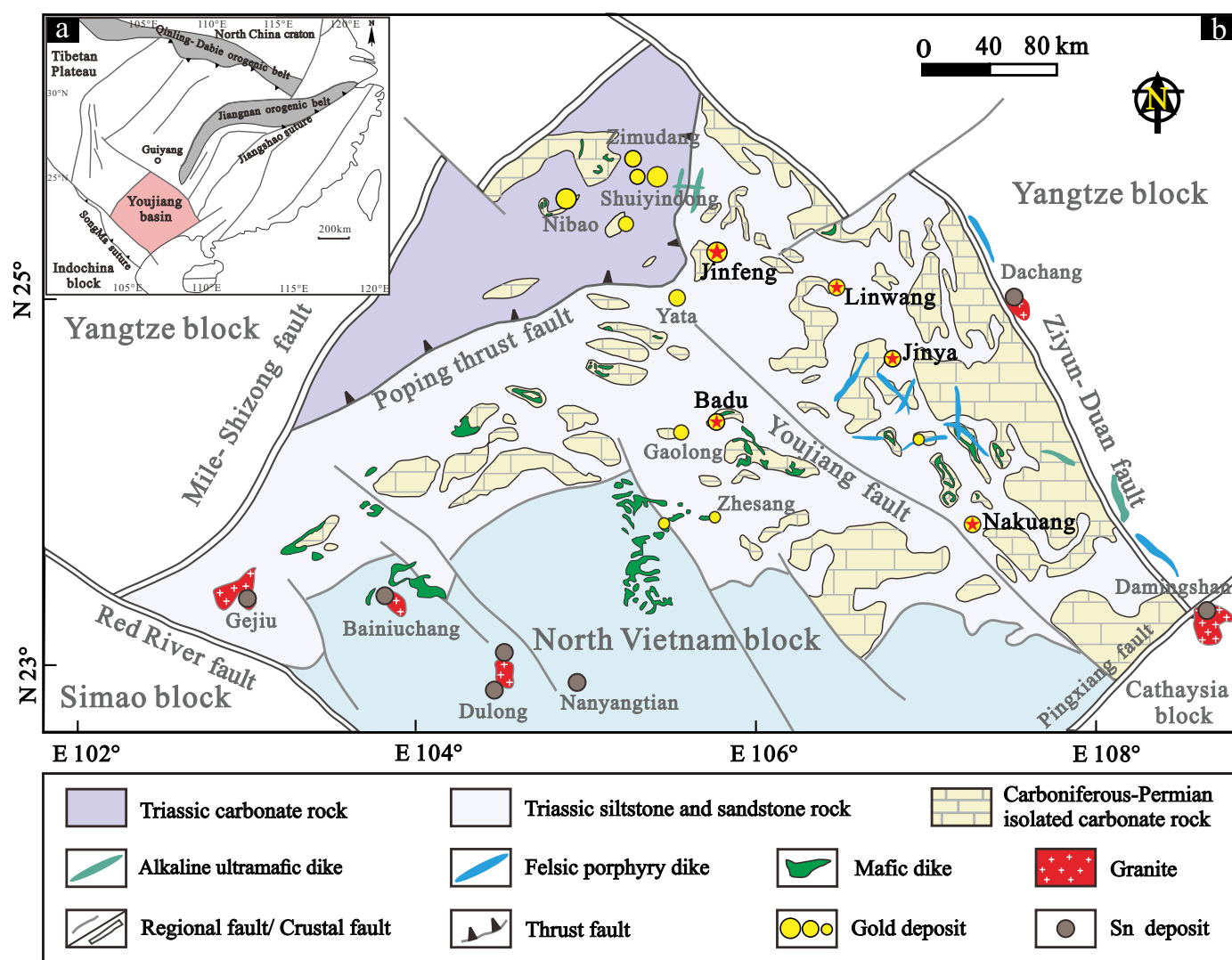


Fig. 1. (a) A simplified tectonic map of the South China block and adjacent regions showing the location of the Youjiang basin. (b) A geologic map of the Youjiang basin showing the distribution of Carlin-type gold deposits and granite-related Sn polymetallic deposits (modified from Xie et al., 2018).

tion from the late Permian and Early Triassic subduction to Middle-Late Triassic collision along the southwestern margin of the South China block (Qiu, L., et al., 2017). Structural analyses reveal that the basin was affected by Late Triassic north-south shortening and uplift associated with formation of the EW-trending top-to-the-north Youjiang fold-and-thrust belt. This was followed by Cretaceous top-to-the-northwest thrusting and fault propagation folding, and then by Cenozoic NE-SW-trending extensional normal faults (Qiu et al., 2016).

The basin records significant marine sedimentation between the late Paleozoic and Early Triassic (Song et al., 2009), leading to formation of an ~7-km-thick sequence of marine sediments (Yang et al., 2012). Then, uplift and erosion of the Indosinian orogen shed voluminous siliciclastic turbidites into the basin, forming the Middle Triassic strata (Cai and Zhang, 2009; Yang et al., 2012; Hu et al., 2017). The oldest strata in the basin is Cambrian carbonate that crops out within the core of an anticline. The Permian and Triassic strata, composed of limestone, dolostone, siltstone, sandstone, and mudstone, are widely distributed throughout the basin (Fig. 1b). In general, the metamorphic grade of rocks in the basin is relatively low, with only low-grade burial metamorphism recorded by the sedimentary sequences (Suo et al., 1998).

Igneous rocks are exposed in places within the basin (Fig. 1b) and mainly consist of basalts and dolerites in the northwestern and southern parts of the basin (ca. 260 Ma; Zhou et al., 2006; Fan et al., 2008) and Late Triassic postcollisional magmatism in the Funing-Napo region (ca. 230–205 Ma; Pi et al., 2016; Jiang et al., 2017; Gao, 2018). Sparse Middle Jurassic high-Mg andesite (ca. 160 Ma; Gan et al., 2016) and Late Cretaceous alkali ultramafic dikes and felsic dikes (ca. 100–84 Ma; Chen et al., 2009b, 2012, 2014; Liu et al., 2010; Zhu et al., 2017) are distributed in southwestern Guizhou and northwestern Guangxi provinces. Additionally, some ca. 100 to 80 Ma granites and granite-related W-Sn polymetallic deposits are present in the southern and eastern margins of the basin (Liu et al., 2007; Cheng et al., 2009, 2010; Feng et al., 2010).

Many low-temperature hydrothermal gold, antimony, and mercury deposits are distributed within the basin and along its northeastern margin (Fig. 1b), among which Carlin-type gold deposits are economically the most important (Hu et al., 2017). Recently, more than 200 Carlin-type gold deposits or occurrences with proven gold reserves of over 800 t have been found or mined, making the basin the second largest Carlin-type gold province in the world (Hu et al., 2017; Su et al., 2018). The deposits occur in clusters along NE- and NW-striking faults and can be divided into three types: stratabound, fault-bound, and compound (Chen et al., 2011; Hu et al., 2017). The stratabound deposits mainly occur in the northwestern part of the basin, with ore hosted in permeable reactive bioclastic limestone or along unconformities in anticlines, such as Shuiyindong. The fault-bound deposits, such as Lannigou and Jinya, are mainly distributed in the southeastern part of the basin and commonly occur along high-angle reverse faults and adjacent altered rocks, with ore hosted in calcareous siltstone, sandstone, and mudstone. The compound deposits, such as Nibao and Linwang, are controlled by strata and faults, with ore hosted in fracture zones and permeable reactive strata. Although the ore controls vary, most deposits have mineral assemblages, alteration types, elemen-

tal associations, and ore-forming conditions similar to those of Carlin-type gold deposits in Nevada, USA (Hu et al., 2002, 2017; Su et al., 2009a, 2018). Additionally, some unique gold deposits, such as the largest, Badu, which is mainly hosted in altered dolerite or its fault contact with adjacent sedimentary rocks, are recognized in the southern part of the basin (Dong, 2017; Gao, 2018; Su et al., 2018).

## Deposit Geology

### *The Badu deposit*

The Badu gold deposit is located near the Youjiang fault, which divides the basin into northern and southern parts (Fig. 1b). Recent exploration drilling defined a proven gold reserve of 35 t (1.13 Moz) with an average gold grade of 2 g/t (0.07 oz/t) according to the internal 2018 exploration report of Jinfeng Mining Company, making it the largest dolerite-hosted gold deposit in the basin. Badu together with Gaolong and the newly discovered Nabi deposit constitute the Gaolong-Badu gold belt. Detailed geologic characteristics of the Badu deposit have been described by Gao (2018). A brief summary follows.

The deposit is located on the western flank of the Badu anticline, which was produced by multiple tectonic events, forming a dome-like complex anticline (Yang et al., 2018). From west to east, the direction of the major axis changes from northeast-east trending to east-west and northwest trending, forming a characteristic arc-shaped superposed fold with northward arcuate axis. The whole anticline is crosscut by numerous faults parallel to the fold axis, suggesting they formed simultaneously. Seismic profile interpretation across the anticline shows that the deep structure is dominated by a NE-striking duplex, whereas middle and shallow levels are characterized by N-directed imbricates with fault-related folds (Yang et al., 2018). The structural style and deformation sequence are analogous to the D<sub>1</sub> deformation characteristics recorded in the Youjiang fold-and-thrust belt (Qiu et al., 2016). Devonian rocks occur in the core and Permian to Middle Triassic rocks on the limbs of the anticline (Fig. 2a), which suggests that the fold and related faults formed after the Middle Triassic. Dolerites occupy faults in the core and limbs of the anticline. Early 1:50,000-scale geologic mapping divided the dolerites into three stages (BGMRGX, 1992), but their absolute ages were not determined.

The Lower Devonian Yujiang Formation is dominated by thick layered mudstone and siltstone intercalated with limestone and dolomite that contain disseminated and nodular pyrite. The Upper Devonian Liujiang Formation consists of chert interbedded with tuff and lenses of banded limestone. The Carboniferous strata mainly consists of mudstone and chert. The lower-middle Permian Sidazhai Formation consists of limestone interbedded with chert and is locally marbled and dolomitized. The upper Permian Linghao Formation consists of mudstone, argillaceous sandstone, and tuff intercalated with siliceous mudstone. The Lower and Middle Triassic Shipao Formation and Baifeng Formation are dominated by sandstone, siltstone, and mudstone.

Dolerite is mainly emplaced into Devonian, Carboniferous, and Permian sedimentary strata (Fig. 2a). Obvious intrusive contacts are recorded between the dolerites and the folded sedimentary strata (Fig. 3a) such that sedimentary rocks are slightly metamorphosed. In places, undeformed dolerites

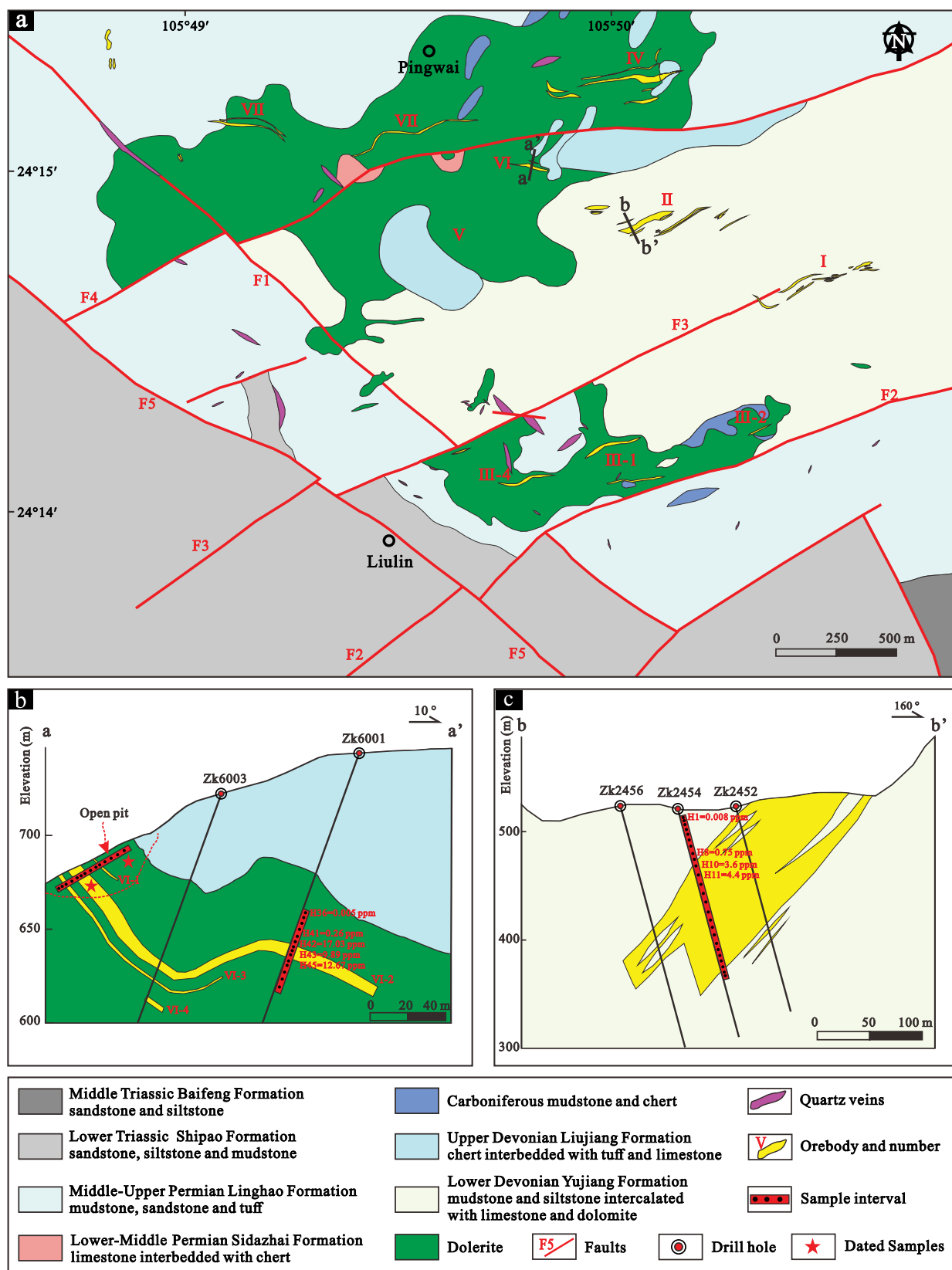


Fig. 2. (a) Schematic geologic map of the Badu gold deposit with locations of orebody VI and II cross section lines a-a' and b-b'. (b) Geologic cross sections of the dolerite-hosted No. VI orebody (a-a') and the sedimentary rock-hosted No. II orebody (b-b') in the Badu deposit (modified from Jinfeng Corp, unpub. report, 2018). Gold grades of samples in drill hole Zk6001 and Zk2454 are from the internal 2018 exploration report of the Jinfeng Mining Company.

enclose folded strata (Fig. 3b). Field observations show that dolerites are controlled by NEE- and NW-trending faults that crosscut the anticline and the Middle Triassic Baifeng Formation. Thus, the dolerites were emplaced after the Middle Tri-

assic. However, the dolerites were disrupted by subsequent faulting that localized gold mineralization.

Badu contains seven major orebodies with tabular shapes or veins. Most orebodies are northeast-east trending with

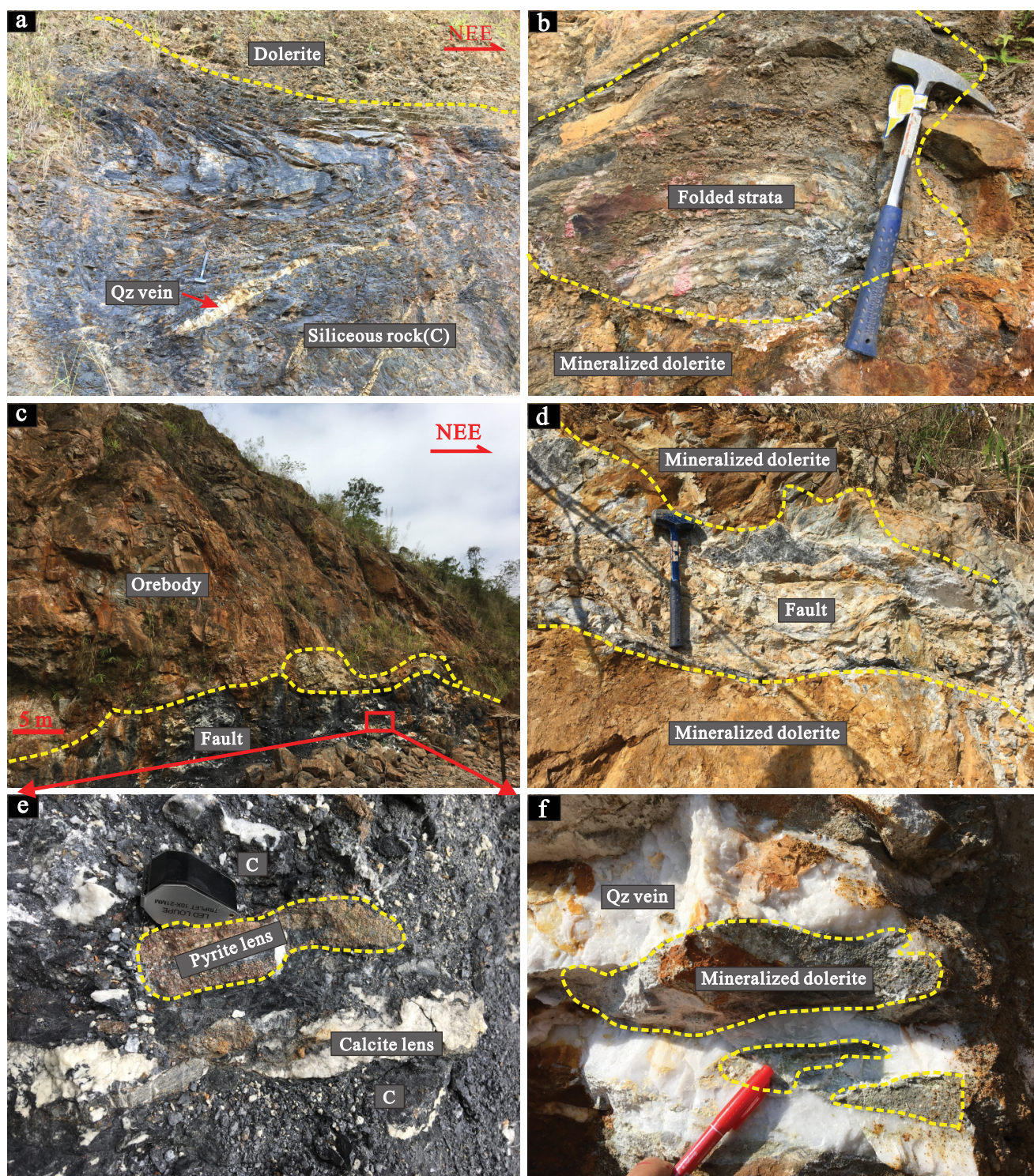


Fig. 3. Photographs representative of outcrops in the Badu deposit. (a) Intrusive contact between dolerite and folded sedimentary strata. (b) Mineralized dolerite with enclave of folded sedimentary rock. (c, d) Mineralized dolerite cut by fault filled with black carbonaceous matter and white calcite. (e) Enlarged picture of red box from (c), showing pyrite lens within carbonaceous matter. (f) Milky quartz veins enveloping centimeter-sized breccia fragments of altered dolerite. Abbreviations: C = carbonaceous matter, Qz = quartz.

minor northwest trending and are controlled by secondary faults. Each orebody contains sets of parallel veins (Fig. 2a), with individual vein widths from 2 to 70 m and strike lengths between 10 and 500 m. Drill intercepts show that mineralized veins can extend ~200 m below the surface (Fig. 2b, c). The No. III to VII orebodies constitute 70% of gold resources and are mainly hosted in altered dolerites intersected by fault zones or occur along faulted contacts between dolerites and sedimentary strata (Fig. 3c, d). The No. I and II orebodies constitute less than 30% of gold resources and are principally hosted in mudstone, siltstone, and sandstone of the Lower Devonian Yujiang and upper Permian Linghao Formations (Fig. 2c). The average gold grades of each orebody vary from 1 to 6 g/t; the No. VI orebody is the richest with local grades up to 20 g/t.

Faults that intersect dolerite and faulted contacts between dolerites and strata are typically filled by graphitic calcite veins (Fig. 3c, d). Gold is associated with lenses of pyrite in these veins (Fig. 4e), but grades are commonly less than 1 g/t. On each side of the faults, dolerites are fractured and altered, but the density of fracturing and intensity of alteration progressively decreases with increasing distance from the faults. Hydrothermal fluids probably flowed along the faults and penetrated into the fractured dolerite. Some mineralized dolerites contain abundant milky quartz veins with widths up to 20 cm. Quartz veins locally envelop fragments of centimeter-sized altered dolerite that has been sheared and brecciated (Fig. 3f). However, the quartz veins are not mineralized.

Least altered dolerite is green in color and has a porphyritic texture with phenocrysts of pyroxene and plagioclase (Fig. 5a). Mineralized dolerite is bleached and intensely altered because of strong fluid-rock interaction (Fig. 5c). Hydrothermal alteration is characterized by disseminated pyrite and arsenopyrite, which are the major gold-bearing ore minerals (Fig. 5b-e). Fe sulfides constitute <5 to 20 vol % of the mineralized dolerites. The relative proportions of pyrite and arsenopyrite are spatially variable in different orebodies; samples with more arsenopyrite have lower gold grades. For example, the richest No. VI orebody with gold grades up to 20 g/t is dominated by pyrite (Fig. 5c-e), whereas the No. VII orebody is dominated by arsenopyrite and generally has gold grades less than 2 g/t (Fig. 5b). However, there are no apparent correlations between amount and size of pyrite and gold grade, but samples with higher gold grades are usually associated with very fine grained pyrite (“dust pyrite”), which is nearly invisible in hand specimens (Fig. 5e). Although strongly altered, mineralized dolerite contains hardly any hydrothermal quartz grains, but samples from faults intersecting dolerite exhibit obvious silicification and carbonization (Fig. 5f). In contrast, silicification is primarily expressed as quartz or quartz-ankerite veinlets that crosscut mineralized dolerite (Fig. 5g-j). Adjacent to the veinlets, pyrite grains are coarse, up to 1 cm, and form pyrite aggregates (Fig. 5h-j). In most cases, Fe sulfides are disseminated in altered host rocks but are not recorded in quartz veins or veinlets, which suggests that fluid-rock interaction was the major mechanism of gold precipitation. In mineralized dolerite, plagioclase is altered to sericite. In addition, clusters of hydrothermal sericite are locally distributed in quartz-ankerite veinlets that are cut by quartz veinlets (Fig. 5h, i). Another distinct characteristic of mineralized dolerite

is that coarse-grained pyrite and arsenopyrite are crosscut by graphitic carbon veinlets (Fig. 5g). These veinlets may be hydrothermal in origin or consist of bitumen derived from sedimentary strata.

#### *The Jinfeng, Linwang, Jinya, and Nakuang deposits*

The Jinfeng, Linwang, Jinya, and Nakuang deposits in the northern part of the Youjiang fault (Fig. 1b) are mainly hosted in the Middle Triassic calcareous siltstone, mudstone, and silty mudstone. Given the similarity of the four deposits and to avoid repetition of information already in the literature, simplified descriptions of the main features of each deposit are summarized in Table 1.

Four deposits are all located on the eastern margin of the Permian to Lower Triassic platform carbonates. The stratigraphy exposed in these deposits is similar and composed of two distinct sequences: isolated carbonate platforms that are dominated by thin-bedded limestones of the Permian and Lower Triassic, and deep basin facies that are composed of calcareous sandstone and siltstone with interlayered mudstone of the Middle Triassic (Chen et al., 2010, 2011, 2015; Xie et al., 2018). Gold mineralization is primarily hosted in the Middle Triassic dolomitic carbonaceous siltstone and mudstone (Table 1; Fig. 4). Orebodies occur as veins and lenses and are structurally controlled by secondary faults (Fig. 4), which produced ore with brecciated and stockwork textures (Fig. 5n, o). No dolerite dikes have been identified in these deposits by geologic mapping or drilling. The nearest igneous rocks are the NW-trending Jiayou and NE-trending Naling felsic dikes, which are ~35 km from the Jinya deposit.

Ore samples collected from the four deposits are characterized by a dense distribution of disseminated sulfides in silicified calcareous siltstone (Fig. 5l-o). Pyrite is the only ore mineral in Jinfeng and Linwang. Arsenopyrite and minor pyrite are predominant in Jinya and Nakuang. Locally, silicified and mineralized calcareous siltstone is crosscut by milky quartz veinlets that contain little or no sulfides (Fig. 5n, o). Given that ore samples with quartz veinlets are spatially associated with higher-grade ore, we infer that the veinlets are related.

#### **Mineral Paragenesis and Alteration**

Samples collected along transects that extend from barren rocks through the orebodies—e.g., sample intervals of open pit and drill hole Zk6001 from the No. VI orebody (Fig. 2b)—were examined to identify pre-ore-, ore-, and late ore-stage minerals (Fig. 6) and to document the hydrothermal alteration types associated with gold mineralization.

#### *Dolerite-hosted ore of the Badu deposit*

*Pre-ore stage:* The least altered dolerite is mainly composed of plagioclase (~50 vol %), clinopyroxene (~45 vol %), minor titanite and ilmenite (~5 vol %), trace apatite, rare sulfides, and quartz (Fig. 6), and is characterized by typical doleritic or poikilophitic texture with laths of plagioclase intergrown with clinopyroxene (Fig. 7a). The phenocrysts of plagioclase and clinopyroxene are weakly altered to sericite and chlorite, and the matrix has a muddy appearance due to its fine grain size. Energy dispersive spectrometry (EDS) semiquantitative results show that clinopyroxene is Ti bearing. Titanite is inter-

grown with plagioclase and clinopyroxene (Fig. 7b). Two types of ilmenite can be identified; one occurs as lamellae in titanite crystals with orientations in three directions with 60° angle, and the other forms as coarse crystals that contain inclusions of plagioclase and clinopyroxene (Fig. 7b, c). Tiny chalcopyrite, sphalerite, and pyrite are enclosed within titanite, occur

as strings along the boundary of titanite, or are sporadically scattered in the matrix.

*Ore stage:* In altered and mineralized dolerite, primary minerals and textures have been intensively replaced and obscured because of fluid-rock interaction. Magmatic clinopyroxene, plagioclase, titanite, and ilmenite are completely

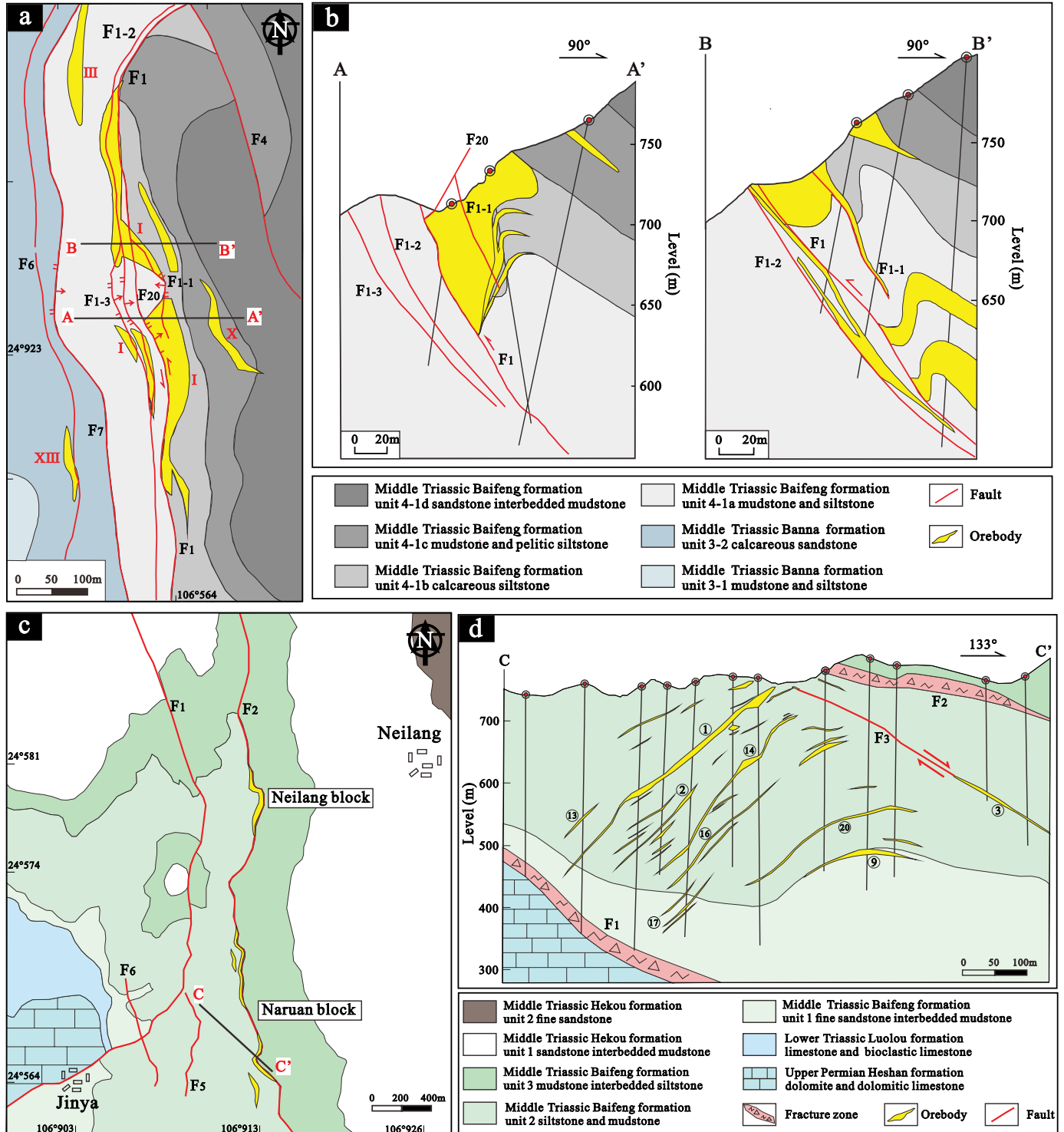


Fig. 4. Schematic geologic maps and representative cross sections of the Linwang (a, b; modified from Chen et al., 2010) and Jinya (c, d; modified from Chen et al., 2015) gold deposits.



Table 1. Major Geologic Features of the Badu, Jinfeng, Linwang, Jimya, and Nakuang Deposits in the Youjiang Basin

Deposit	County, Province	Reserves (t)	Grade (g/t)	Host rocks	Hosting strata	Alterations	Ore minerals	Gangue minerals	References
Badu	Tianlin, Guangxi	35	2	Dolerite/carbonaceous mudstone	?Youjiang Formation of Lower Devonian (D <sub>1y</sub> )	Carbonation, decarbonation, silicification, sulfidation, argillization	Arsenian pyrite, arsenopyrite, stibnite, realgar, orpiment	Quartz, ankerite, calcite, sericite, illite, rutile, Fe-free dolomite	Jinfeng Corp. unpub. report (2018); this study
Jinfeng	Zhenfeng, Guizhou	108.9	3.8	Dolomitic carbonaceous siltstone	Xuman and Bianyang Formations of Middle Triassic (T <sub>2xm</sub> <sup>3,4</sup> , T <sub>2by</sub> )	Decarbonation, silicification, sulfidation, argillization	Arsenian pyrite, arsenopyrite, stibnite, realgar, orpiment	Quartz, calcite, illite, Fe-free dolomite	Chen et al. (2011); Xie et al. (2018)
Linwang	Leye, Guangxi	>20	2.5	Dolomitic carbonaceous siltstone and mudstone	Baifeng Formation of Middle Triassic (T <sub>2bf</sub> <sup>4,la,b,c</sup> )	Decarbonation, silicification, sulfidation, argillization	Arsenian pyrite, arsenopyrite, stibnite, realgar, orpiment	Quartz, calcite, illite, Fe-free dolomite	B.X. Chen, pers. commun. (2017); this study
Jimya	Fengshan, Guangxi	35	3	Dolomitic carbonaceous siltstone and mudstone	Baifeng Formation of Middle Triassic (T <sub>2bf</sub> <sup>2</sup> )	Decarbonation, silicification, sulfidation, argillization	Arsenian pyrite, arsenopyrite, stibnite, realgar, orpiment	Quartz, calcite, illite, Fe-free dolomite	Chen et al. (2015); China Geology Survey (2015)
Nakuang	Tiandong, Guangxi	10	2	Dolomitic carbonaceous siltstone and mudstone	Baifeng Formation of Middle Triassic (T <sub>2bf</sub> <sup>2,2,2-3</sup> )	Decarbonation, silicification, sulfidation, argillization	Arsenian pyrite, arsenopyrite, stibnite, realgar, orpiment	Quartz, calcite, illite, Fe-free dolomite	Wu (2018); this study

altered to sericite (~45 modal %), carbonate (mainly ankerite) (~45 vol %), pyrite (~15 vol %), arsenopyrite (~10 vol %), rutile (~3 vol %), apatite (~1 vol %), minor base metal sulfides (~1 vol %), and trace monazite (Fig. 7d, e). On the basis of micro and microtextural relationships of altered minerals, alteration and mineralization can be divided into three stages (Fig. 6): an early ankerite + sericite + rutile alteration stage (I), the main pyrite + arsenopyrite + quartz + ankerite + sericite + apatite + monazite alteration stage (II), and a late quartz + carbonate + (sulfide) + (barite) stage (III). Ankerite alteration is marked by pervasive replacement of primary pyroxene, plagioclase, and titanite by ankerite (Fig. 7e, f). It affected all or most altered dolerite dikes including those with low grades (<1 g/t), which indicates that ore-forming fluids were carbonic. Such fluids may have been reduced to form the graphitic veinlets that crosscut mineralized dolerite and the graphitic calcite veins along faults. Sericite alteration is best developed in primary plagioclase. Ankerite is overgrown by sericite (Fig. 7f), which suggests that sericite is slightly later. Alternatively, given that alteration mimics the poikilohitic texture of clinopyroxene and plagioclase, ankerite and sericite alteration may be nearly synchronous. The main ore stage II has been further subdivided into substages II-1 and II-2. Substage II-1 is represented by sulfidation, resulting in widespread dissemination of pyrite and arsenopyrite in the matrix of altered minerals (Fig. 7d, e). The absence of overgrowth or replacement relationships suggests that these sulfides coprecipitated. Pressure shadows of quartz and ankerite develop around some of the pyrite crystals (Fig. 7g), implying a compression condition after pyrite formation and gold mineralization. Most of the pyrite grains have an inclusion-rich anhedral core, followed by an inclusion-free outer rim (Fig. 7h). The most common mineral inclusions identified in the pyrite cores are ankerite, sericite, and rutile (Fig. 7h), which implies that the pyrite cores formed during or after ankerite and sericite. The pyrite rims appear to have formed in open space. Backscattered electron (BSE) images and EDS semiquantitative analyses of the pyrite cores and rims reveal compositional variations in As contents, but both are arsenian pyrite. In contrast, arsenopyrite is homogeneous. Electron probe microanalysis (EPMA) and laser ablation-inductively coupled plasma-mass spectrometry (LA-ICP-MS) analyses suggest that gold is mainly incorporated into the lattice of arsenian pyrite and arsenopyrite as invisible gold (Gao, 2018). Substage II-1 was the main period of gold deposition. Locally, mineralized dolerite is crosscut by quartz-ankerite veinlets. Arsenian pyrite and arsenopyrite with the aforementioned core-rim textures are locally enclosed within veinlets, which suggest that the veinlets are synchronous with, or slightly later than, sulfidation. Additionally, hydrothermal apatite grains and sericite clusters also occur in these veinlets that are isolated or intergrown with arsenian pyrite and arsenopyrite (Fig. 7i).

Substage II-2 is represented by Sb-Cu-bearing and base metal sulfides, including stibnite, tetrahedrite, tennantite, chalcopyrite, and sphalerite. They characteristically occur as strings or fillings along the microfractures in pyrite (Fig. 7j), as aggregates or scattered grains in quartz veinlets, or as infillings along fractures in quartz-ankerite veinlets (Fig. 7k). It is noteworthy that substage II-2 is confined to mineralized dolerite and closely follows substage II-1; both are cut by late

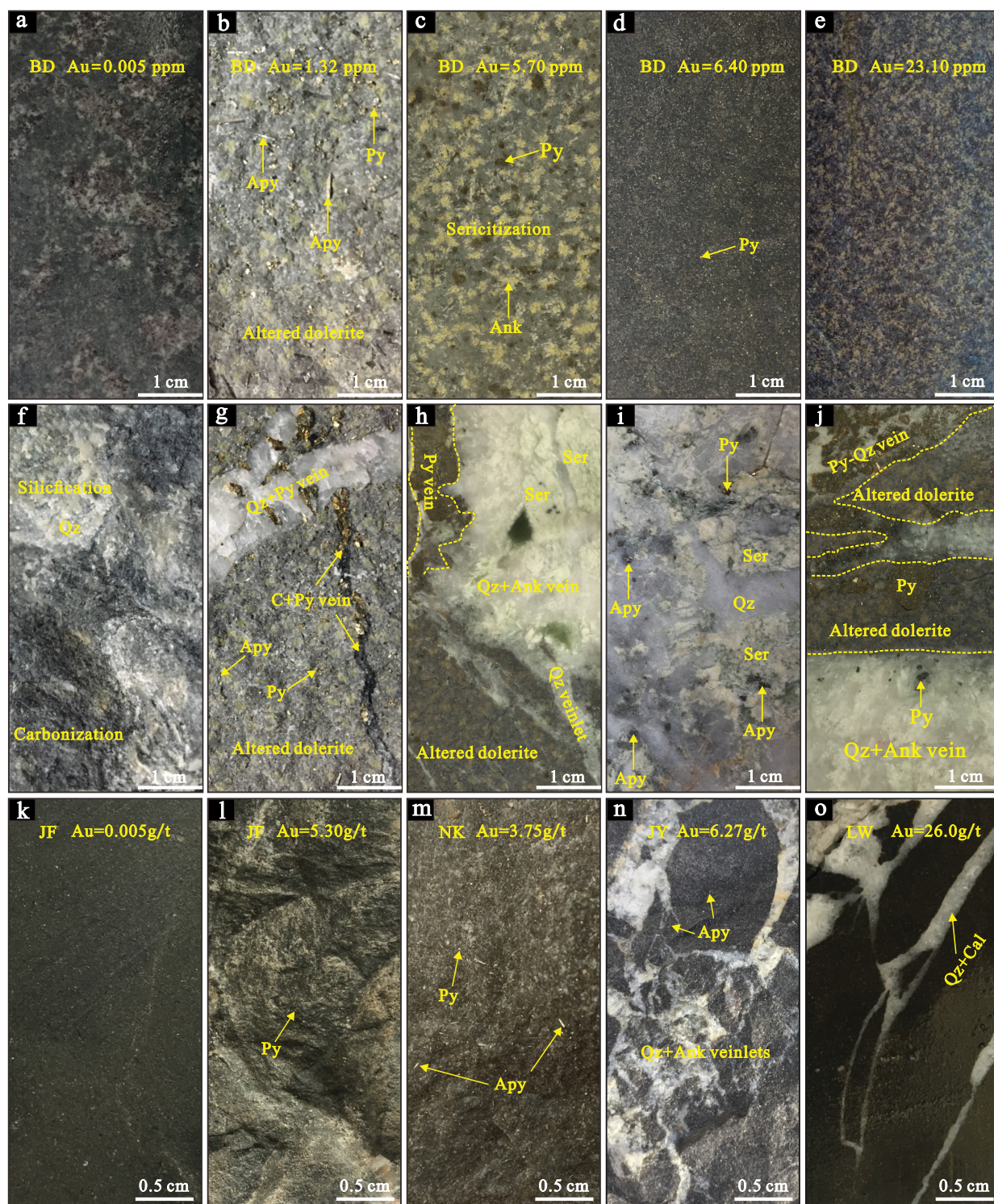


Fig. 5. Photographs of hand specimens from the Badu deposit (a-j) and Jinfeng, Linwang, Jinya, and Nakuang deposits (k-o). (a) Least altered dolerite with porphyritic texture. (b-e) Disseminated pyrite and arsenopyrite in mineralized dolerites with variable gold grade. (f) Silicified dolerite with abundant carbonaceous matter. (g) Mineralized dolerite crosscut by quartz veins and solid carbonaceous material veinlets. (h, i) Mineralized dolerite crosscut by quartz-ankerite veins with clots of hydrothermal sericite. (j) Altered dolerite cut by pyrite-quartz veinlet and quartz-ankerite vein containing pyrite. (k) Barren dolomitic calcareous siltstone and (l) ore-grade silicified calcareous siltstone with disseminated pyrite from the Jinfeng deposit. (m) Ore-grade silicified calcareous siltstone with disseminated arsenopyrite and pyrite from the Nakuang deposit. (n) Brecciated ore-grade silicified calcareous siltstone with abundant disseminated arsenopyrite cemented by quartz-ankerite from the Jinya deposit. (o) High-grade silicified calcareous siltstone crosscut by quartz-calcite veinlets from the Linwang deposit. Abbreviations: Ank = ankerite, Apy = arsenopyrite, BD = Badu, C = carbonaceous matter, Cal = calcite, JF = Jinfeng, JY = Jinya, LW = Linwang, NK = Nakuang, Py = pyrite, Qz = quartz, Ser = sericite.

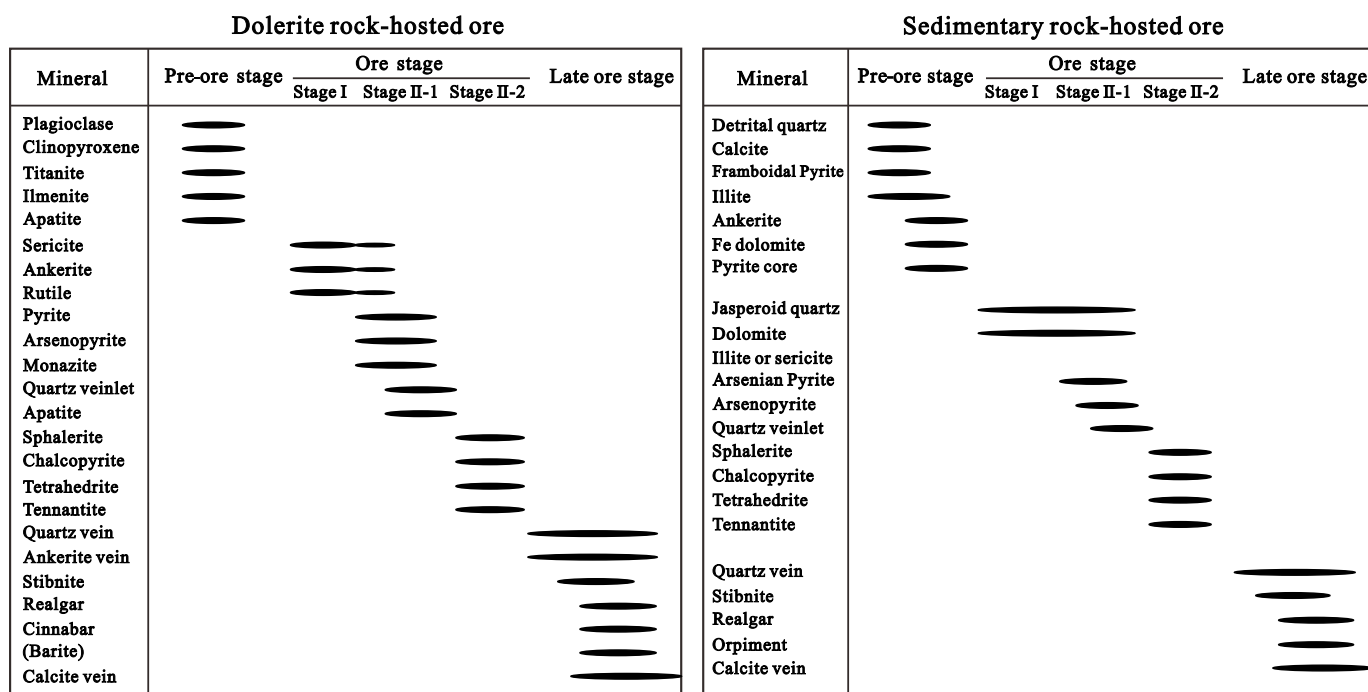


Fig. 6. Mineral paragenesis for dolerite rock-hosted (Badu) and sedimentary rock-hosted (Jinfeng, Linwang, Jinya, Nakuang, and Badu) gold deposits in the Youjiang basin.

ore-stage veinlets, suggesting that substage II-1 and II-2 belong to an evolving ore stage. Precipitation of sulfosalt and base metal sulfides may have been promoted by cooling and pH increase after consumption of Fe, S, As, and Au from ore fluids by sulfidation of dolerite during stage II-1.

**Late ore stage:** Pre-ore and ore stages are cut by multiple generations of late veinlets containing quartz, ankerite, and calcite, with remaining open space filled by trace amounts of stibnite, realgar, cinnabar, and barite. However, the As-Sb-Hg sulfides and barite generally do not occur together. Locally, barite occurs as veinlets with widths of ~1 mm that crosscut previous stages (Dong, 2017). Multiple stages of precipitation of quartz and ankerite are indicated by mutually crosscutting relationships (Fig. 7l).

#### Mudstone-hosted ore of the Badu deposit

The No. II orebody is hosted in mudstones of the Lower Devonian Yujiang Formation. Samples with variable alteration and gold grades ranging from 0.008 to 4.40 g/t were collected from drill core ZK2454 (Fig. 2c). Petrographic examinations reveal that hydrothermal alteration related to gold mineralization consists of carbonate dissolution, silicification, argillization, and sulfidation.

**Pre-ore stage:** The sample assayed at 0.008 ppm Au (H<sub>1</sub>, Fig. 8a) is composed of abundant ankerite that is distributed in a clastic matrix of extremely fine grained detrital quartz and illite (Fig. 8b). The ankerite has irregular and zigzag margins, displays compositional zoning, and contains numerous mineral inclusions (Fig. 8c). Locally, it occurs as veins or veinlets that crosscut mudstone. Framboidal pyrite is commonly disseminated in the matrix.

**Ore stage:** A low-grade altered sample with 0.75 ppm Au (H<sub>8</sub>, Fig. 8d) contains disseminated pyrite and arsenopyrite.

Ankerite is still common but has been partially replaced by quartz with abundant tiny residual inclusions of ankerite (Fig. 8e, f). The ankerite is patchy because of replacement and has obvious zoning with darker rims surrounding lighter cores, due to the lower Fe content of the rims. The darker rim is in contact with hydrothermal quartz, which allows that Fe in pre-ore-stage ankerite was released during replacement.

In a mineralized sample with 4.40 ppm Au (H<sub>11</sub>, Fig. 8g), most of the ankerite is replaced by hydrothermal quartz with a jasperoid texture (Fig. 8h). Illite occurs as inclusions in quartz and penetrates or crosscuts quartz (Fig. 8i), which suggests that they formed simultaneously. Minor amounts of Fe-free dolomite are also present. Fe-free dolomite occurs in contact with, and contains tiny inclusions of, ankerite (Fig. 8i), suggesting it formed by replacement of ankerite. Hydrothermal pyrite, the major gold-bearing sulfide, is significantly more abundant compared to the low-grade sample. EPMA and LA-ICP-MS data show that the pyrite is arsenian and contains gold in its lattice (W. Gao, unpub. data, 2020). Arsenian pyrite is mainly distributed along the boundary of quartz grains. Small amounts of arsenian pyrite are also enclosed within quartz and nonferroan dolomite grains, indicating that arsenian pyrites were trapped during quartz crystal growth. The consistent association of gold-bearing arsenian pyrite and hydrothermal quartz suggests that they are contemporaneous and formed from a single stage (II-1).

As in substage II-2 of the dolerite-hosted ore, late sulfosalt and base metal sulfides, including stibnite, tetrahedrite, tennantite, chalcocopyrite, and sphalerite, fill microfractures in gold-bearing arsenian pyrite (Fig. 8j).

**Late ore stage:** Coarse-grained stibnite and intergrowths of realgar and orpiment occur within fractures on the periphery of gold orebodies or locally in vugs and open space

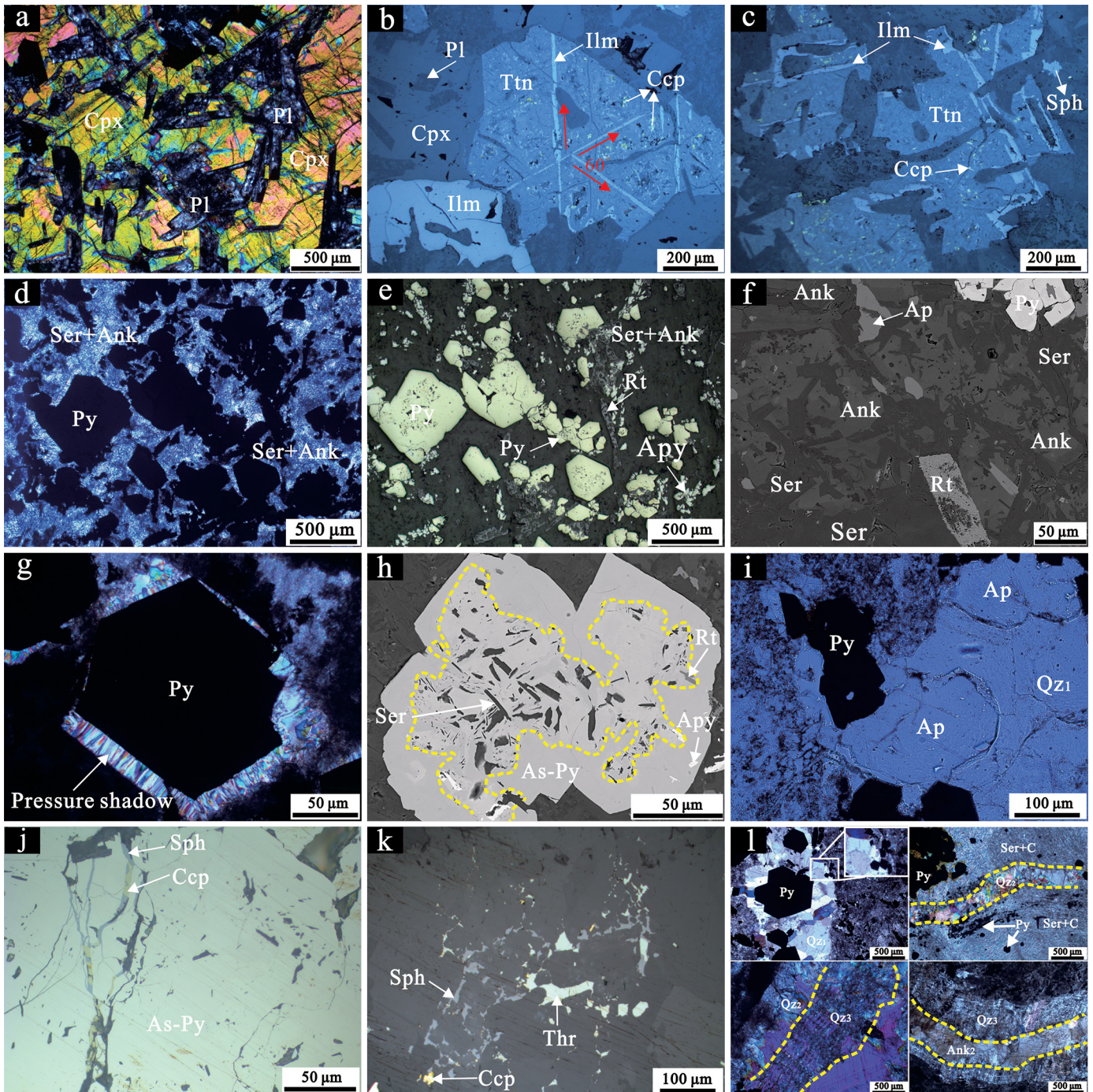


Fig. 7. Photomicrographs showing alteration features and mineral paragenesis of dolerite-hosted orebodies in the Badu deposit. (a) Least altered dolerite showing typical doleritic or poikilophitic texture with laths of plagioclase intergrown with clinopyroxene. (b, c) Two types of ilmenite in least altered dolerite. (d, e) Mineralized dolerite with ore-stage pyrite, arsenopyrite, rutile, ankerite, and sericite. (f) Ore-stage ankerite and sericite pseudomorphs of the poikilophitic texture of clinopyroxene and plagioclase. (g) Late ore-stage pressure shadow of quartz and ankerite around pyrite. (h) Ore-stage gold-bearing arsenian pyrite with mineral inclusion-rich core and clean rim. (i) Intergrowths of arsenian pyrite and apatite in ore-stage quartz-ankerite veinlet. (j) Sphalerite and chalcopyrite filling fracture in ore-stage pyrite. (k) Sphalerite, tetrahedrite, and chalcopyrite filling the fracture of ore-stage quartz-ankerite veinlet. (l) Multiple stages of quartz-ankerite veinlets with mutually crosscutting relationships. (a, d, g, l) Crossed-polarized light. (i) Plane-polarized light. (b, c, e, h, j, k) Reflected light. (f) BSE image. Abbreviations: Ank = ankerite, Ap = apatite, Apy = arsenopyrite, C = carbonaceous matter, Ccp = chalcopyrite, Cpx = clinopyroxene, Ilm = ilmenite, Pl = plagioclase, Py = pyrite, Qz = quartz, Rt = rutile, Ser = sericite, Sph = sphalerite, Thr = tetrahedrite, Ttn = titanite.

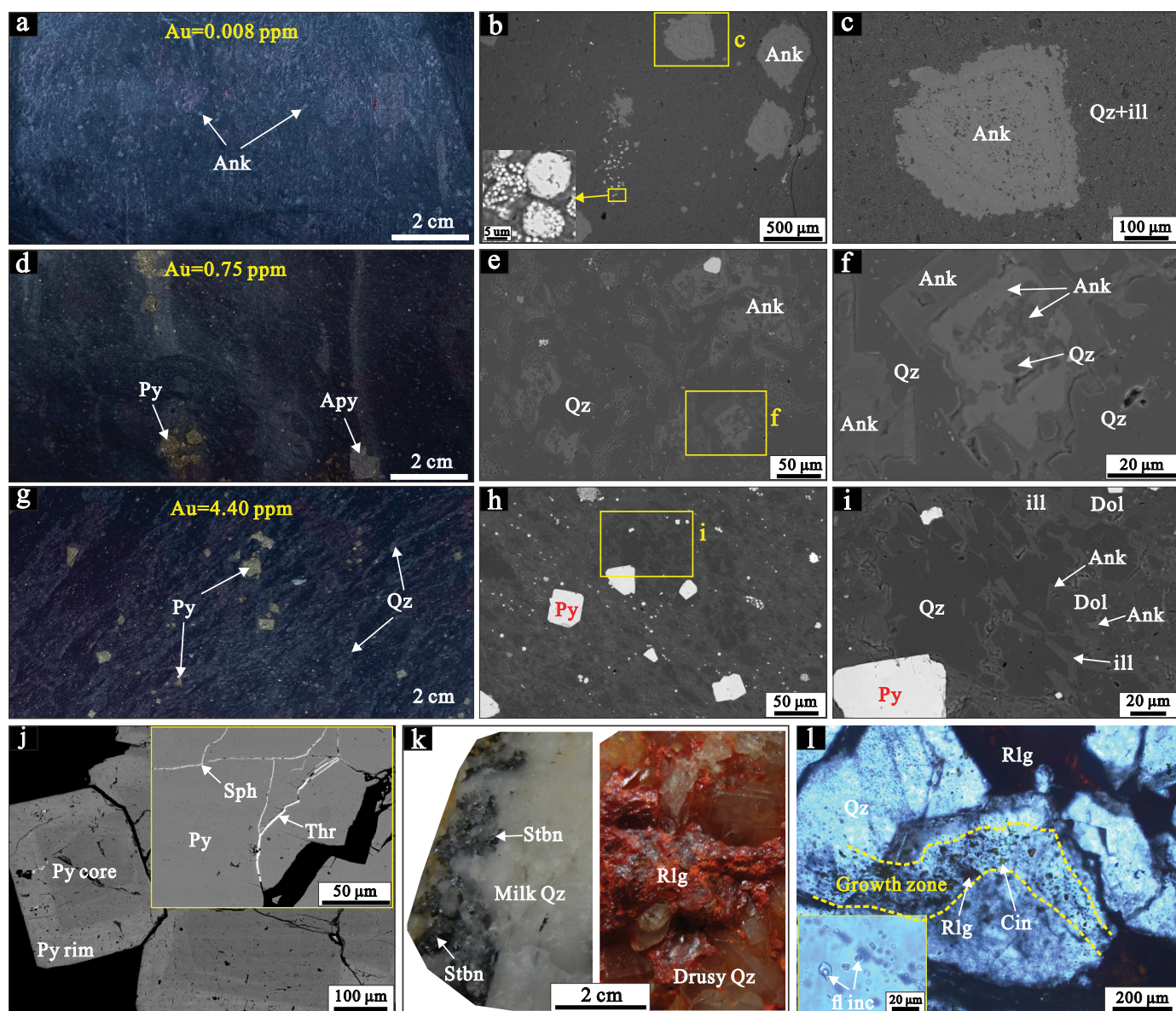


Fig. 8. Photographs (a, d, g, k), BSE images (b, c, e, f, h-i), and plane-polarized light photograph (l) of variably altered and mineralized samples from the No. II orebody of the Badu deposit hosted in mudstone of the Lower Devonian Yujiang Formation. (a-c) Unaltered mudstone with 0.008 ppm Au containing coarse grains of ankerite with abundant mineral inclusions in a fine-grained matrix of quartz and illite with framboidal pyrite. (d-f) Altered mudstone with 0.75 ppm Au containing ankerite that is partially replaced and rimmed by dark ankerite and quartz. (g-i) Mineralized mudstone with 4.40 ppm Au containing disseminated pyrite and relict ankerite that is strongly replaced by quartz, illite, and dolomite. (j) Ore-stage pyrite with core-rim texture and sphalerite, chalcopyrite, and tetrahedrite along the fractures. (k) Late ore-stage stibnite in a milky quartz vein and realgar intergrown with drusy quartz crystals. (l) Quartz grain intergrown with realgar with abundant fluid and some realgar and cinnabar inclusions. Abbreviations: Ank = ankerite, Apy = arsenopyrite, Cin = cinnabar, Dol = dolomite, fl inc = fluid inclusion, Ill = illite, Py = pyrite, Qz = quartz, Rlg = realgar, Sph = sphalerite, Stbn = stibnite, Thr = tetrahedrite.

with euhedral quartz crystals (Fig. 8k), suggesting that they precipitated by cooling (Hofstra and Cline, 2000). Quartz intergrown with stibnite and realgar contains abundant small fluid inclusions, giving it a wispy and turbid appearance under transmitted light. Fluid inclusions are CO<sub>2</sub> rich (Fig. 8l). Some quartz crystals have turbid cores containing fluid inclusions and clear rims with multiple growth zones that are intergrown with realgar and cinnabar (Fig. 8l), indicating they formed simultaneously. Thus, late ore-stage euhedral quartz

formed before, during, and probably after realgar and cinnabar precipitation.

#### *Sedimentary rock-hosted ore of the Jinfeng, Linwang, Jinya, and Nakuang deposits*

At the microscopic scale, the Jinfeng, Linwang, Jinya, and Nakuang deposits share comparable mineral assemblages and textures (Fig. 6). To avoid repetition, a simplified paragenesis with supporting evidence is provided below.

**Pre-ore stage:** The barren samples with 0.005 ppm Au from the four deposits are dominated by abundant Fe-bearing dolomite and quartz, minor dolomite, calcite, pyrite, carbonaceous matter, and trace muscovite and apatite (Fig. 9a). Fe-bearing dolomite contains 9 to 15 wt % Fe based on EDS analyses and is characterized by compositional zoning with numerous mineral inclusions (Fig. 9d). Framboidal pyrite and anhedral to euhedral pyrite with core-rim texture were identified by BSE imaging. However, nanoSIMS mapping and LA-ICP-MS analyses show that such pyrite is barren of gold (Xie et al., 2018; W. Gao, unpub. data, 2020).

**Ore stage:** Mineralized samples from the four deposits are characterized by a dense distribution of disseminated pyrite or arsenopyrite and by a marked decrease in Fe-bearing dolomite and an increase in hydrothermal quartz (Fig. 9b, c). In detail, early calcite has been completely dissolved, and Fe-bearing dolomite is gradually penetrated and replaced by hydrothermal quartz that contains residual Fe-bearing dolomite inclusions. Sulfide contents and gold grade have a positive relationship with the intensity of alteration: relict Fe-bearing dolomite is common in altered samples with low gold grades (Fig. 9e) but is intensively replaced by hydrothermal quartz in mineralized samples (Fig. 9f). Additionally, the dolomite inclusions in hydrothermal quartz are Fe poor (Fig. 9f). Silicification is also expressed by the formation of quartz veinlets that contain trace sulfides (Fig. 9g).

The replacement of Fe-bearing dolomite by pyrite and/or arsenopyrite and Fe-poor dolomite (Fig. 9e, f) suggests that they formed by sulfidation. Pyrite is the major ore mineral in the Jinfeng and Linwang deposits (Fig. 9c), but arsenopyrite and pyrite are preponderant in the Jinya and Nakuang deposits (Fig. 9g). Both sulfides are mainly distributed along the boundaries of or enclosed within hydrothermal quartz grains, indicating they formed during hydrothermal quartz growth. This consistent spatial association suggests that they formed during a single stage from similar ore fluids.

Under BSE imaging with high contrast and low brightness, pyrite is characterized by distinct compositional zoning. The core resembles the anhedral to euhedral pyrite in barren samples, suggesting it is pre-ore stage. Ore pyrite primarily occurs as 10- to 50- $\mu\text{m}$ -thick overgrowths on pre-ore pyrite and is distinguished by relatively smoother surface, much higher As contents, and multiple discrete bands with different As contents (Fig. 9h). At Jinya and Nakuang, pyrite cores have a sieve texture indicative of dissolution that is infilled and overgrown by ore-stage pyrite (Fig. 9i). Ore-stage pyrite also occurs as isolated grains less than 30  $\mu\text{m}$  in diameter that lack pre-ore pyrite cores. Arsenopyrite intergrown with arsenian pyrite from Jinya and Nakuang has a homogeneous appearance under BSE images but generally contains mineral inclusions of pyrite with sieve texture and detrital material of host rock (Fig. 9i). Nano-SIMS and LA-ICP-MS analyses suggest ore-stage pyrite rims and arsenopyrite contain elevated As, Au, Sb, Hg, Tl, and Cu contents (Yan, J., et al., 2018; Xie et al., 2018; Wu, 2018; W. Gao, unpub. data, 2020).

**Late ore stage:** Paragenetically late realgar commonly fills fractures that crosscut ore-stage quartz veinlets and mineralized rock (Fig. 9j, k). Locally, realgar, orpiment, and/or stibnite form coarse-grained and euhedral crystals in vugs intergrown with drusy quartz or calcite (Fig. 9l). Calcite, the most ubiqu-

itous gangue mineral, generally occurs as euhedral crystals intergrown with realgar, orpiment, and stibnite. Calcite also occurs as veins or veinlets that crosscut all previous minerals, representing the waning stage of the hydrothermal systems.

### Sampling and Analytical Methods

The analytical objectives, analytical contents, and sampling information are described in Table 2. The sites and detailed descriptions of samples for zircon U-Th/He dating are provided in Table 3. During sampling, material with crosscutting veins or veinlets were avoided as cautiously as possible to minimize the potential effects of post-ore hydrothermal events. Magmatic zircon and hydrothermal rutile for U-Pb dating were separated through conventional crushing, sieving, density and magnetic separation, and handpicking under a binocular microscope. It is important to note that we did not use any heating methods, and all samples were dried at room temperature during separation because of the thermal sensitivity of zircon U-Th/He system.

#### *Whole-rock major, trace element, total sulfur, and Au-As-Sb-Hg analyses*

Major and trace element analyses were performed using PANalytical Axios-advance (Axios PW4400) X-ray fluorescence spectrometer (XRF) and PerkinElmer Sciex ELAN 6000 ICP-MS, respectively, at the State Key Laboratory of Ore Deposit Geochemistry, Institute of Geochemistry, Chinese Academy of Sciences. The analytical precision was generally better than 5%. Gold, arsenic, antimony, mercury, and total sulfur were analyzed at the ALS-Chemex (Guangzhou) commercial laboratories. Au contents were obtained by fire assay fusion, total sulfur was obtained with a Leco sulfur analyzer, and Hg contents were determined atomic fluorescence spectrometry (AFS). As, Ag, and Hg contents were analyzed by ICP-atomic emission spectrometry and ICP-MS. Detailed analytical methods are described in Appendix 1.

#### *EPMA major and minor element analyses of rutile*

Chemical analyses of rutile were conducted using a JEOL JXA-8230 electron probe microanalyzer at Shandong Bureau Testing Center of China Metallurgical Geology Bureau (Jinan). The analyses were performed using a 15-kV accelerating voltage, a 20-nA beam current, and a 5- $\mu\text{m}$  beam spot diameter. Detailed analytical and correction methods are described in Appendix 1.

#### *Zircon U-Th/He dating*

Only eight of 14 samples yielded enough suitable zircon grains for U-Th/He dating, which was conducted in the Arizona Radiogenic Helium Dating Laboratory at the University of Arizona. The analytical procedure has been described by Reiners et al. (2004) and Reiners (2005) and is summarized in Appendix 1.

#### *SIMS zircon, rutile, and monazite U-Pb dating*

In situ zircon, rutile, and monazite U-Th-Pb dating were conducted using a Cameca IMS-1280HR SIMS at the Institute of Geology and Geophysics, Chinese Academy of Sciences in Beijing, China. Detailed descriptions of instrument parameters and analytical methods for zircon, rutile, and monazite

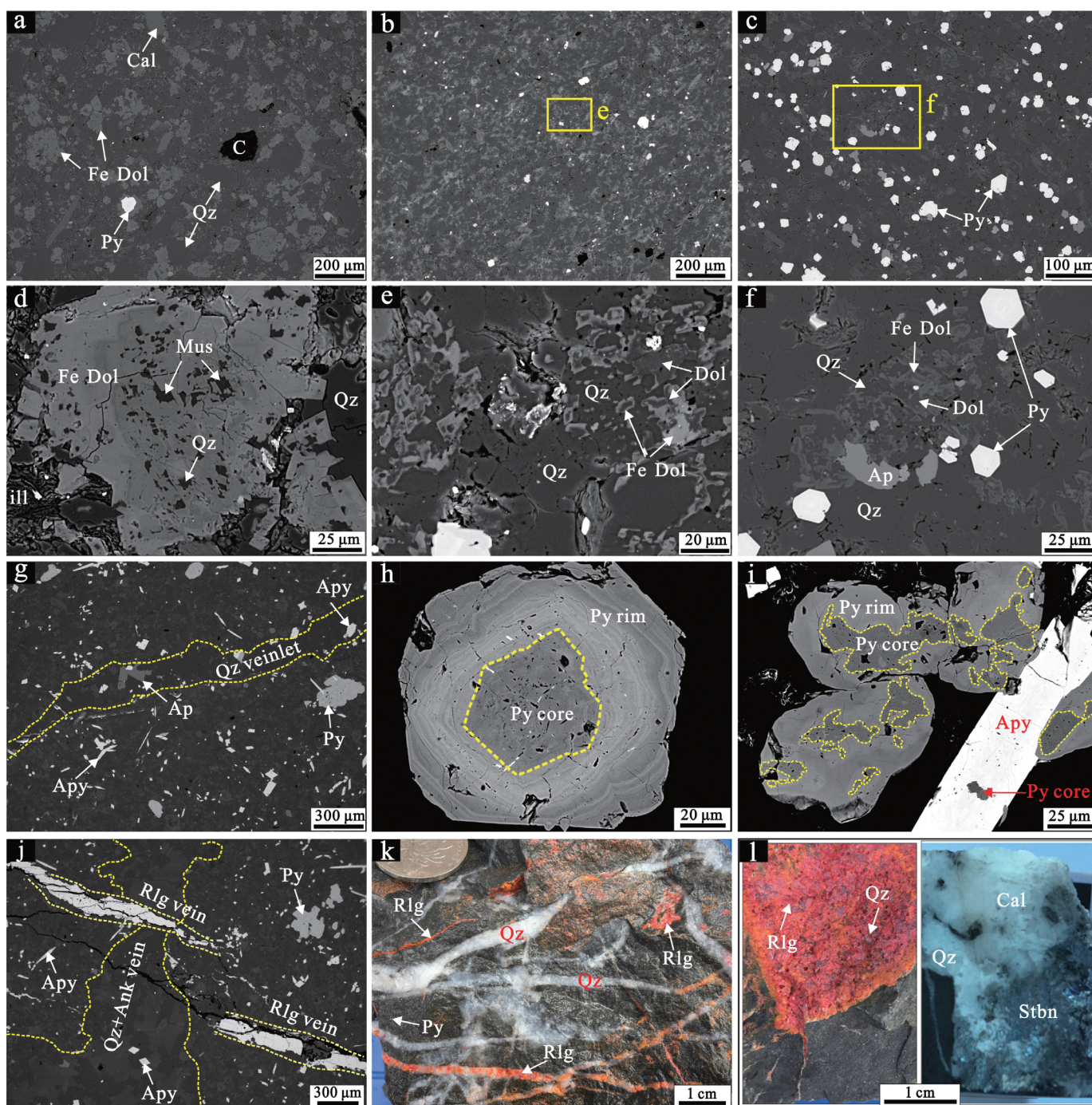


Fig. 9. BSE images (a–j) and photographs (k, l) of variably altered and mineralized samples from the Jinfeng, Linwang, Jinya, and Nakuang Carlin-type gold deposits. (a, d) Barren siltstone with  $<0.005$  ppm Au composed of quartz and ferroan dolomite with minor dolomite, calcite, pyrite, and carbonaceous matter. Ferroan dolomite cores contain numerous mineral inclusions of muscovite and quartz. (b, e) Low-grade siltstone with  $<1$  ppm Au consisting of ferroan dolomite that is partially replaced by quartz; calcite is absent. (c, f) Ore-grade siltstone with  $>3$  ppm Au containing abundant pyrite and relict ferroan dolomite that is intensively replaced by quartz. (g) Mineralized siltstone with abundant arsenopyrite and pyrite is crosscut by quartz veinlets containing little or no sulfides. (h) Euhedral dark pyrite core and bright oscillatory zoned arsenian pyrite rim. (i) Corroded dark pyrite core rimmed by bright arsenian pyrite and arsenopyrite. (j, k) Mineralized siltstone and ore-stage quartz-ankerite veinlets cut by late realgar veinlets. Note coin for scale in k. (l) Open-space-filling realgar intergrown with drusy quartz and stibnite intergrown with calcite and quartz. Abbreviations: Ank = ankerite, Ap = apatite, Apy = arsenopyrite, C = carbonaceous matter, Cal = calcite, Dol = dolomite, Fe-Dol = Fe-bearing dolomite, Ill = illite, Mus = muscovite, Py = pyrite, Qz = quartz, Rlg = realgar, Stbn = stibnite.

Table 2. Detailed Analytical Contents and Sampling Information in This Study

Deposit	Objective	Content	Sample number/weight	Location
Badu	Revealing element associations and mineralization processes	Whole-rock major, trace element, total sulfur, and Au-As-Sb-Hg analyses	43 dolerite specimens with variable gold grades	Ore zones of surface exposures and drill cores (Fig. 2b)
Badu	Emplacement age of dolerite	Magmatic zircon U-Th-Pb dating	One least altered dolerite sample of ~30 kg	Open pit of No. VI orebody (Fig. 2b)
Badu	Mineralization age	Hydrothermal rutile U-Th-Pb dating	One mineralized dolerite sample of ~30 kg	Open pit of No. VI orebody (Fig. 2b)
Badu	Mineralization age	Hydrothermal monazite U-Th-Pb dating	32 mineralized dolerite specimens	Open pit of No. VI orebody (Fig. 2b)
Jinfeng, Linwang, Jinya, Nakuang, Badu	Lower limit on mineralization age	Detrital zircon U-Th/He dating	14 mineralized samples, each ~15–30 kg	Open pits, underground workings, and drill cores

Table 3. Detailed Information of the 14 Samples Collected for Zircon U-Th/He Dating from the Badu, Jinfeng, Linwang, Jinya, and Nakuang Deposits

Deposit	Sample	Lithology and strata	Sample location	Description	Zircon U-Th/He
Jinfeng	JF-1	Calcareous siltstone of T <sub>2by</sub>	520 m, orebody at open pit	5.38 g/t; silicification; amounts of fine-grained pyrite	Yes
	JF-2	Calcareous siltstone of T <sub>2xm</sub>	250 m, orebody at underground	4.65 g/t; silicification; amounts of fine-grained pyrite	Yes
	JF-3	Calcareous siltstone of T <sub>2by</sub>	520 m, orebody at open pit	4.25 g/t; silicification; amounts of fine-grained pyrite	No
Linwang	LW-1	Silty mudstone of T <sub>2bf</sub>	710 m, I2 orebody at open pit	6.80 g/t; silicification; amounts of fine-grained pyrite	No
	LW-2	Calcareous siltstone of T <sub>2bf</sub>	710 m, I2 orebody at open pit	10.50 g/t; silicification; amounts of fine-grained pyrite	Yes
	LW-3	Calcareous siltstone of T <sub>2bf</sub>	760 m, I2 orebody at open pit	22.60 g/t; silicification; amounts of fine-grained pyrite	Yes
Jinya	JY-1	Calcareous siltstone of T <sub>2bf</sub>	660 m, orebody at underground	4.50 g/t; silicification; amounts of arsenopyrite	Yes
	JY-2	Calcareous siltstone of T <sub>2bf</sub>	580 m, orebody at underground	3.78 g/t; silicification; amounts of arsenopyrite	No
Nakuang	NK-1	Sandstone of T <sub>2bf</sub>	650 m, orebody at open pit	0.87 g/t; silicification; amounts of pyrite	Yes
	NK-2	Mudstone of T <sub>2bf</sub>	650 m, orebody at open pit	3.40 g/t; black in color; silicification; arsenopyrite > pyrite	No
	NK-3	Calcareous siltstone of T <sub>2bf</sub>	500 m, orebody at drill hole	6.00 g/t; silicification; amounts of arsenopyrite	Yes
Badu	BD-1	Dolerite	675 m, VI orebody at open pit	12.70 g/t; bleached; sericitization; amounts of pyrite	Yes
	BD-2	Dolerite	620 m, VII orebody at open pit	3.05 g/t; bleached; sericitization; amounts of pyrite	No
	BD-3	Mudstone of D <sub>1y</sub>	460 m, II orebody at drill hole	4.40 g/t; black in color; silicification; amounts of pyrite	No

can be found in X.H. Li et al. (2009) and Q.L. Li et al. (2011, 2013b), respectively. An O<sup>2-</sup> primary ion beam was accelerated at 13 kV. The ellipsoidal spots are about 10 × 15 μm in diameter for zircon and monazite, and 20 × 30 μm in diameter for rutile. A mass resolution of ~5,400 (at 10% peak height) for zircon, ~5,400 (defined at 10% peak height) for monazite, and ~7,000 (defined at 10% peak height) for rutile were used to separate Pb<sup>+</sup> peaks from isobaric interferences. A single electron multiplier was utilized to measure the secondary ion intensity by peak jumping mode. Each measurement consists of seven cycles and the total analytical time is ~15 min. Detailed analytical and calibration procedure and common Pb correction methods are supplied in Appendix 1.

## Results

### Lithochemistry of variably altered dolerite

Results of whole-rock major and trace elements, total sulfur, and Au-As-Sb-Hg analyses are provided in Appendix Tables A1 and A2. In Figure 10a-f, the major and trace element contents of samples with different gold grades are displayed to characterize changes associated with alteration and mineralization of dolerite. When the Fe and S contents are normalized to Al contents (Hofstra and Cline, 2000), mineralized samples (Au > 0.01 ppm) extend upward toward the pyrite line (Fig. 10a), which suggests that gold-bearing pyrite precipitated by sulfidation of Fe-bearing minerals (Su et al., 2009a). The Al<sub>2</sub>O<sub>3</sub> versus K<sub>2</sub>O diagram (Fig. 10b) shows that

mineralized samples contain more K and extend to the sericite line, which is consistent with sericitization. In contrast, SiO<sub>2</sub> decreases from 45 wt % in barren dolerites to 20 wt % in mineralized samples (Fig. 10c), indicating that SiO<sub>2</sub> was released. In comparison to barren samples (Fig. 10d-f), mineralized dolerites contain higher Au (0.1–23.1 ppm), As (mean >10,000 ppm), Sb (0.8–37 ppm), and Au/Ag ratios (avg value of 26).

Isochron diagrams have been used to identify immobile elements and document gains and losses of elements associated with alteration and mineralization (Grant, 1986; Hofstra and Cline, 2000; Yigit and Hofstra, 2003). Based on this method, a sample with the lowest Au, S, and loss on ignition (LOI) values of 0.003 ppm, 0.07 wt %, and 4.49 wt %, respectively, was chosen as the least altered dolerite. Samples with 2.27, 8.78, and 23.10 ppm Au were selected as mineralized dolerite. The isochron diagram clearly demonstrates that gold mineralization is associated with significant additions of S, Au, As, and Sb and slight additions of Hg and Tl (Fig. 10g), a typical element association for Carlin-type gold deposit (Hofstra and Cline, 2000; Ressel et al., 2000; Hu et al., 2002; Yigit and Hofstra, 2003). Among these, Fe is immobile and Au, S, and As are dramatically introduced, which suggests that gold-bearing arsenian pyrite and arsenopyrite in the ore formed by sulfidation. Other added elements include Rb, Ba, K<sub>2</sub>O, and LOI, which is consistent with sericitic and ankeritic alterations. In contrast, Li, Na<sub>2</sub>O, and SiO<sub>2</sub> are removed. Nearly all of the Na has been removed, which is characteristic of



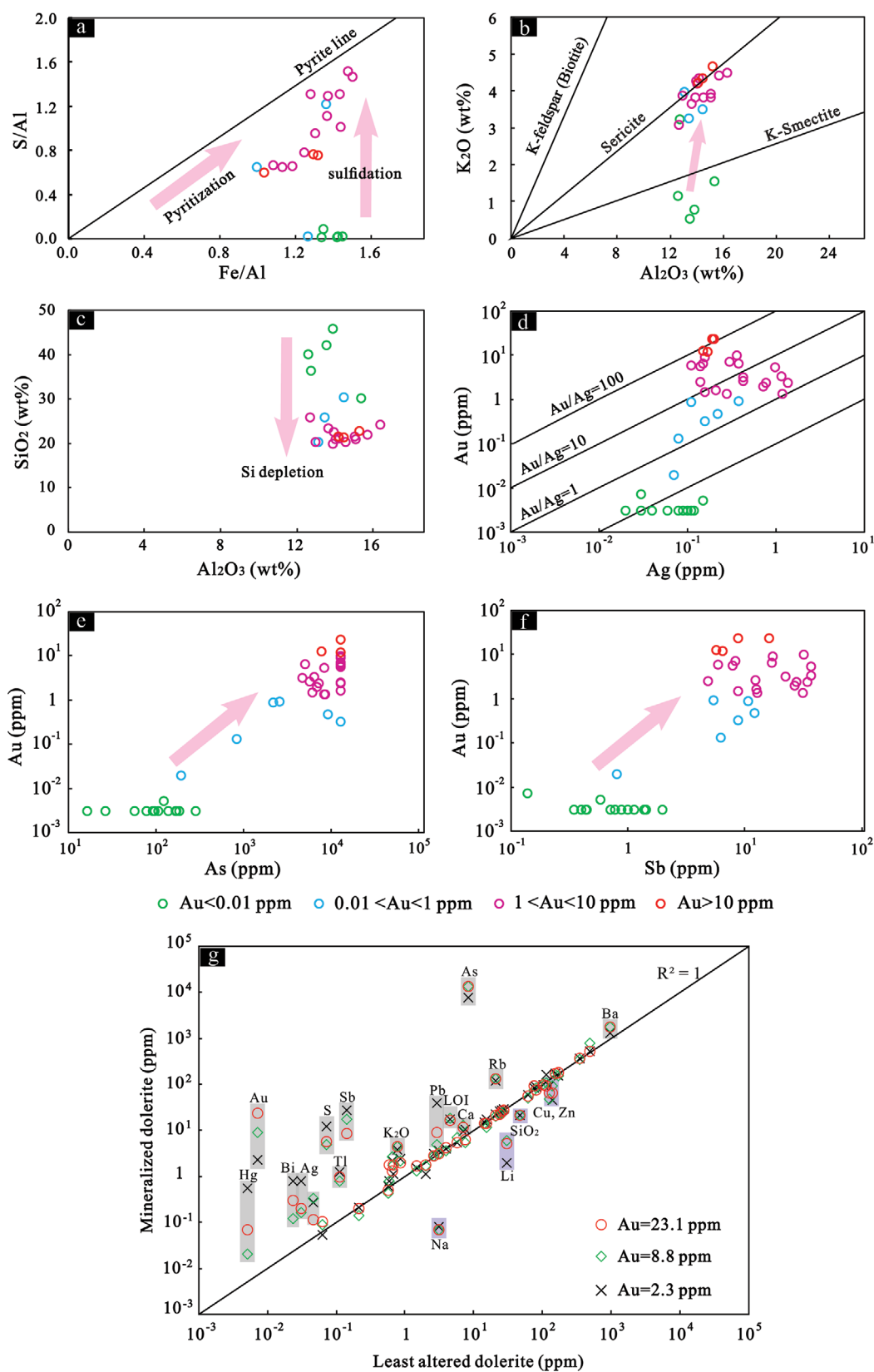


Fig. 10. Alteration plots (a-c), variation plots of selected minor elements (d-f), and isochron diagram (g) in dolerite samples with variable gold grades from the Badu deposit. See text for further description.

altered igneous rocks in Carlin-type gold deposit (Phinisey et al., 1996; Ressel et al., 2000). The depletion of  $\text{SiO}_2$  is distinctive and consistent with the scarcity of quartz grains in mineralized dolerite.  $\text{Al}_2\text{O}_3$ ,  $\text{TiO}_2$ , and  $\text{Fe}_2\text{O}_3$  are immobile, indicating that Fe, a key element for formation of pyrite and gold precipitation, was provided by host rock, consistent with the conclusion that ore formation fluids of Carlin-type deposits contain no Fe (Su et al., 2009a). The base metals, e.g., Cu, Pb, and Zn, remain relatively immobile or weakly depleted, demonstrating that base metal sulfides were scarce, a characteristic feature of Carlin-type gold deposits (Hofstra and Cline, 2000; Ressel et al., 2000; Hu et al., 2002; Yigit and Hofstra, 2003; Su et al., 2018).

### Zircon U-Th/He ages

Results for 23 zircon grains are listed in Table A3 and Figure 11. Three zircon grains from Badu yielded corrected U-Th/He ages of 148 to 121 Ma and a weighted average age of  $137 \pm 20$  Ma ( $2\sigma$ ,  $n = 3$ ). Six zircon grains from Nakuang yielded corrected U-Th/He ages of 141 to 121 Ma and a weighted average age of  $131 \pm 7.4$  Ma ( $2\sigma$ ,  $n = 6$ ). Five zircon grains from Linwang yielded corrected U-Th/He ages of 143 to 126 Ma and a weighted average age of  $133 \pm 6.5$  Ma ( $2\sigma$ ,  $n = 5$ ) after an outlier with low effective uranium concentration (eU = U +  $0.235 \times \text{Th}$ ) was excluded (Fig. 11d). Analogously, five zircon grains from Jinfeng had corrected U-Th/He ages of 161 to

133 Ma and a weighted average age of  $146 \pm 13$  Ma ( $2\sigma$ ,  $n = 4$ ) after an outlier of smaller grain was excluded (Fig. 11c). Zircon grains from these four deposits yielded similar weighted average U-Th/He ages of 146 to 131 Ma. In contrast, zircon grains from Jinya yielded much younger corrected U-Th/He ages of 113.8 to 84.1 Ma and a weighted average age of  $103 \pm 22$  Ma ( $2\sigma$ ,  $n = 3$ ).

### SIMS magmatic zircon U-Pb age

The dated zircon grains are euhedral to subhedral and transparent under transmitted light, are 50 to 100  $\mu\text{m}$  in length, and have aspect ratios of 1:1 to 3:1. Two types of zircon are evident from the CL images: one is relatively homogeneous, with dark-gray cathodoluminescence (CL) and little or no zoning (Fig. 12a, b), similar to magmatic zircon in dolerite; the other has oscillatory zoning, and some grains contain inherited cores.

Fifteen analyses were conducted on 14 zircon grains during a single analytical session; the results are provided in Table A4. They have moderate to high U (212–1,779 ppm) and Th (113–1,862 ppm) contents and Th/U ratios between 0.22 and 1.34. Common Pb is low. Among these, three grains with oscillatory zoning yielded older  $^{206}\text{Pb}/^{238}\text{U}$  ages of  $254.3 \pm 3.8$ ,  $759.5 \pm 10.8$ , and  $2419.7 \pm 30.5$  Ma, which are interpreted as the ages of inherited zircons. One grain with core-rim texture had  $^{206}\text{Pb}/^{238}\text{U}$  ages of  $260.5 \pm 3.9$  and  $207.2 \pm 3.1$  Ma in the

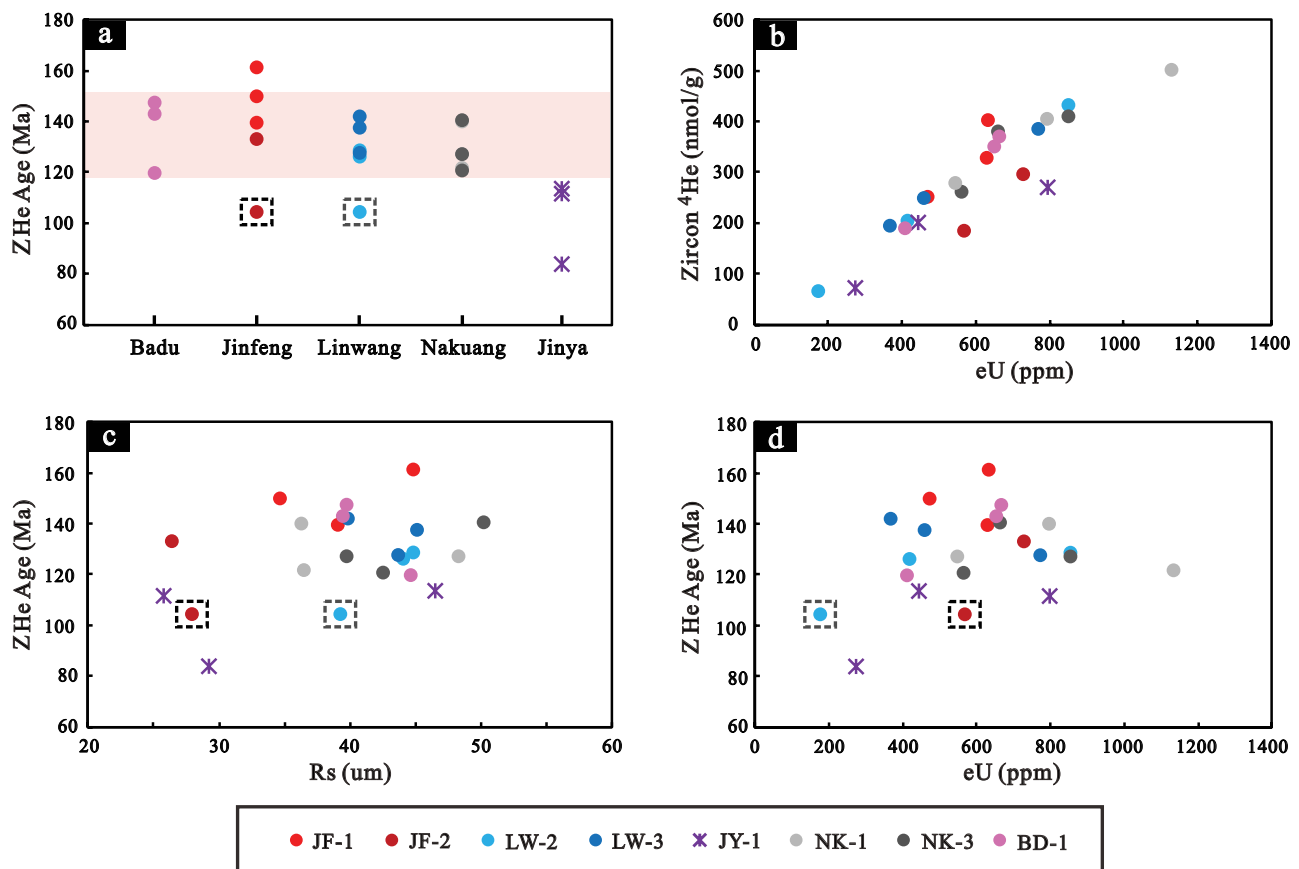


Fig. 11. Summary of zircon U-Th/He ages (a), correlations of eU with  $^4\text{He}$  abundance (b), grain radius with zircon (U-Th)/He ages (c), and eU with zircon (U-Th)/He ages (d) of samples from the Badu, Jinfeng, Linwang, Jinya, and Nakuang deposits. The black and gray dashed boxes emphasize JF-2@1 and LW-1@1 dates, which have lower zircon U-Th/He ages because of smaller size ( $R_s$ ) and/or lower eU.

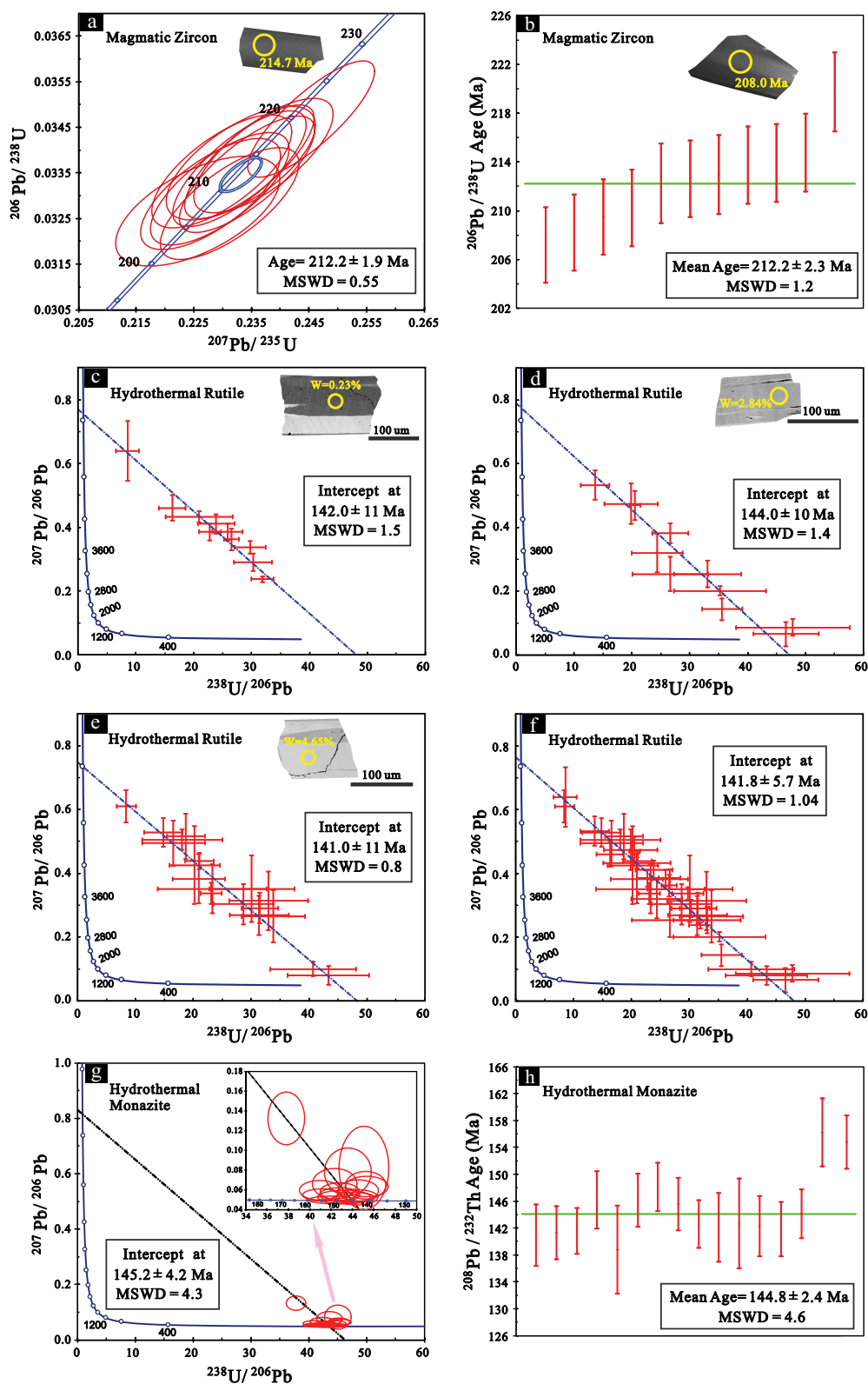


Fig. 12. Dating results of magmatic zircon, hydrothermal rutile, and monazite in the Badu deposit. (a, b) Concordia diagram and weighted mean  $^{206}\text{Pb}/^{238}\text{U}$  age for magmatic zircon from the least altered dolerite (data point uncertainties are  $2\sigma$ ). (c-e) Tera-Wasserburg U-Pb plot for areas with different W, Fe, Nb, and U contents and common Pb compositions in hydrothermal rutile from the mineralized dolerite. (f) Tera-Wasserburg U-Pb plot integrating all data of c, d, and e. (g, h) Tera-Wasserburg U-Pb plot and weighted mean corrected  $^{208}\text{Pb}/^{232}\text{Th}$  age for hydrothermal monazite from the Badu deposit. The inset images in a and b are representative cathodoluminescence images and  $^{206}\text{Pb}/^{238}\text{U}$  ages of zircon. The inset images in c-e are representative high-contrast backscattered electron images and W contents of three types of compositional zoning in hydrothermal rutile.

core and rim, respectively. Eleven zircons with dark-gray and weak CL zoning yielded  $^{206}\text{Pb}/^{238}\text{U}$  ages from  $208.0 \pm 3.1$  to  $219.5 \pm 3.1$  Ma, forming a concordia age of  $212.2 \pm 1.9$  Ma ( $2\sigma$ , mean square of weighted deviates [MSWD] = 0.55), and weighted mean  $^{206}\text{Pb}/^{238}\text{U}$  age of  $212.2 \pm 2.3$  Ma ( $2\sigma$ , MSWD = 1.2) (Fig. 12a, b), which is interpreted as the best estimate of crystallization age for the Badu dolerite. It also places an upper limit on the timing of gold mineralization.

#### *Mineralogical and compositional characteristics of rutile*

In the least altered dolerite with high  $\text{TiO}_2$  contents, clinopyroxene, titanite, and ilmenite constitute the main primary Ti-rich minerals, and no rutile crystals were recorded. Titanite has lamellar exsolutions of ilmenite that are oriented in three directions with a  $60^\circ$  angle (Fig. 7b). In the mineralized dolerite, primary Ti-bearing minerals have been altered to auriferous pyrite, arsenopyrite, ankerite, sericite, and rutile (Fig. 7e). This suggests that rutile is an alteration mineral produced by fluid-rock reaction. In nature, the mineral polymorphs of  $\text{TiO}_2$  occur in three structural states with different crystal parameters: rutile, anatase, and brookite, which can be reliably distinguished using laser micro-Raman spectroscopy (Meinhold, 2010). All grains in this study show the peak positions of standard rutile, which is characterized by bands at wavenumbers 143, 247, 447, and  $612\text{ cm}^{-1}$  (Tompsett et al., 1995; Meinhold, 2010), suggesting rutile is the only polymorph.

Rutile in mineralized dolerite is typically dark in color, occasionally shows a red or orange tint, varies from subhedral to anhedral in shape, and commonly is 20 to  $200\ \mu\text{m}$  in length. It shows close spatial associations with ankerite, sericite, gold-bearing pyrite, and arsenopyrite. In places, needle-like rutile aggregates occur with crystallographic alignments that are oriented in three directions with angle of  $60^\circ$  from each other, to form reticulated rutile. Ankerite is intergrown with rutile and infills the micropores between rutile needles. The reticulated rutile and ankerite mimic the texture of magmatic ilmenite and titanite in dolerite (Figs. 7b, 13a), which is indicative of pseudomorphic replacement. Pyrite cores occur adjacent to or around the intergrowths of reticulated rutile, ankerite, and sericite (Fig. 13b), and in turn, the intergrowths can be traced to or enclose the pyrite core (Fig. 13c). Finally, pyrite cores are frequently riddled with inclusions of rutile, ankerite, and sericite (Figs. 7h, 13d). Pyrite rims lack rutile, indicating it formed later in open space.

Some larger euhedral to subhedral rutile grains enclose and are intergrown with ankerite containing tiny inclusions of rutile (Fig. 13e, f). They mimic the morphology of coarse magmatic ilmenite crystals with inclusions of plagioclase and clinopyroxene (Fig. 7b). Pyrite and/or arsenopyrite, as well as their intergrowths, coat or rim rutile and gradually penetrate inward and replace ankerite along the long axis of the crystals and fractures (Fig. 13e-g). When completely replaced, rutile has a mosaic texture that locally encloses pyrite (Fig. 13h). Other rutile grains are euhedral and enclose tiny inclusions of sulfides and Zr-bearing minerals (Fig. 13i).

High-contrast BSE images show that rutile is characterized by complex compositional zoning, including oscillatory, sectorial, patchy, and irregular (Fig. 12c-e). Subtle zoning is evident at the submicron scale. EPMA spot analyses show that the compositional zoning is mainly due to the variations in W, Fe,

V, Cr, and Nb contents (Table A5). Based on the W contents, three types are defined (Fig. 12c-e): light ( $W > 3.5\text{ wt } \%$ ), gray ( $1.0\text{ wt } \% < W < 3.5\text{ wt } \%$ ), and dark ( $W < 1.0\text{ wt } \%$ ). This result suggests that there are extreme element compositions in a single grain. The light and gray areas are characterized by significantly elevated W, Fe, and Nb contents. In contrast, the dark areas have lower W, Fe, and Nb contents but have higher structurally bounded Si and Cr contents.

#### *SIMS rutile U-Pb age*

In situ SIMS U-Th-Pb results for rutile are listed in Table A6. The compositional zoning of W, Fe, Cr, and Nb is accompanied by variable U and Th contents and common Pb ( $f_{206}$ ) compositions. The dark area contains higher contents of U (1.0–25.6 ppm, avg 9.9 ppm) and Th (3.3–82.3 ppm, avg 29.3 ppm), giving Th/U ratios of 1.4 to 4.2. Common Pb is variably high, with values of  $f_{206}$  ranging from 55.5 to 88.1%. On the Tera-Wasserburg plot, the 10 analyses define a regression line (Fig. 12c) that yielded a lower intercept age of  $142.0 \pm 11$  Ma ( $2\sigma$ , MSWD = 1.5).

The gray and light areas contain generally low levels of U (0.3–4.2 and 0.2–1.3 ppm, avg 1.4 and 0.6 ppm, respectively) and Th (0.1–6.5 and 0.0–2.7 ppm, avg 1.8 and 0.7 ppm, respectively), giving Th/U ratios of 0.0 to 2.3 and 0.1 to 2.7, respectively. Common Pb is variable with values of  $f_{206}$  ranging from 4.1 to 75.7%. Although they have extremely low U contents, the data points for gray ( $n = 11$ ) and light ( $n = 18$ ) areas are distributed along two well-defined regression lines that yielded robust lower intercept ages of  $144.0 \pm 10$  Ma ( $2\sigma$ , MSWD = 1.4) and  $141.0 \pm 11$  Ma ( $2\sigma$ , MSWD = 0.8), respectively (Fig. 12d, e). All three areas yielded similar ages. However, the low and variable U contents and the high common Pb ratios result in lower intercept ages with large uncertainties ( $\sim 8\%$ ). When synthesized, all 39 data points yielded a more precise and robust lower intercept age of  $141.7 \pm 5.8$  Ma ( $2\sigma$ , MSWD = 1.04) and the upper intercept of  $^{207}\text{Pb}/^{206}\text{Pb} = 0.78 \pm 0.05$  for the common Pb composition (Fig. 12f), which is interpreted as the best estimate of the crystallization age of hydrothermal rutile.

#### *Monazite occurrences and SIMS U-Th-Pb dating*

Mineralized samples contain trace anhedral or irregular-shaped and colorless monazite that is generally less than  $10\ \mu\text{m}$  in diameter but ranges in diameter up to 20 to  $50\ \mu\text{m}$ . Monazite is spatially associated with gold-bearing pyrite, ankerite, and sericite. Some tiny monazites (generally  $< 20\ \mu\text{m}$ ), together with sericite, ankerite, and hydrothermal rutile, occur as inclusions enclosed within gold-bearing pyrite, and tiny sericite and arsenian pyrite grains are also contained in monazite (Fig. 14a, b). Some monazite grains grow on the edge of, or in contact with, gold-bearing pyrite (Fig. 14c). More generally, monazite occurs as isolated, clustered, and beaded crystals in ankerite and sericite (Fig. 14d-g). They have irregular and jagged edges and contain inclusions of sericite and pyrite (Fig. 14h). Additionally, some monazite grains contain primary two-phase fluid inclusions (Fig. 14i), consistent with those from ore-stage quartz veinlets (Dong, 2017). All monazite grains are homogeneous and do not show any textures of multistage growth and dissolution and reprecipitation under high-contrast BSE images.

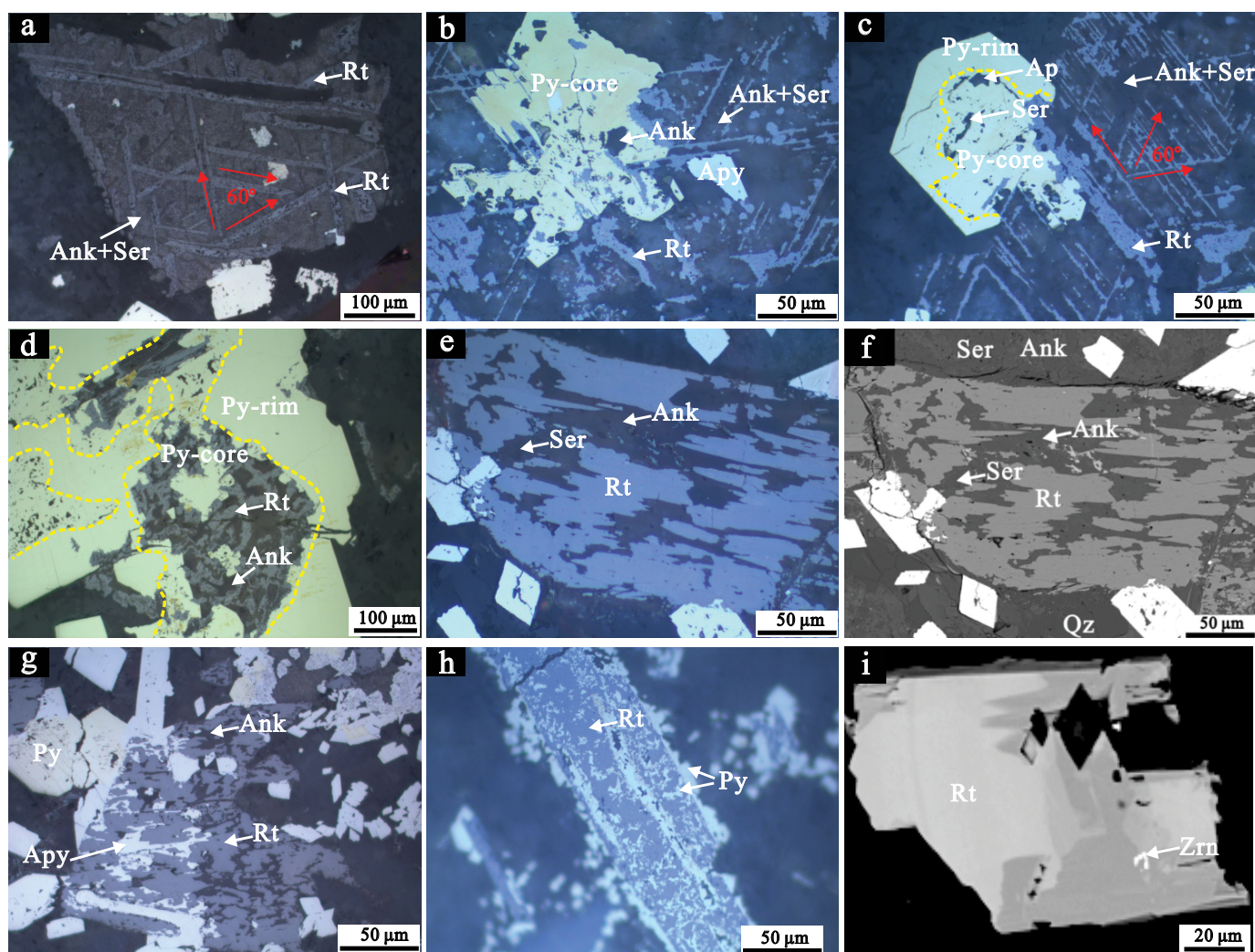


Fig. 13. Photomicrographs in reflected light and backscattered electron images (f, i) showing characteristics of hydrothermal rutile in the Badu deposit. (a) Characteristic reticulated rutile oriented in three directions with angle of  $60^\circ$ . (b, c) Reticulated rutile gradually replaced by pyrite core. (d) Reticulated rutile enclosed in pyrite core. (e, f) Coarse rutile intergrown with hercynite ankerite. (g) Ankerite partially replaced by pyrite and arsenopyrite. (h) Characteristic mosaic rutile. (i) Rutile with complex compositional zoning and a tiny zircon inclusion. Abbreviations: Ank = ankerite, Ap = apatite, Apy = arsenopyrite, Py = pyrite, Qz = quartz, Rt = rutile, Ser = sericite, Zrn = zircon.

In situ SIMS U-Th-Pb results of monazite are provided in Table A7. A total of 16 analyses were conducted on 16 larger grains with homogeneous surface and no inclusions. The monazite contains highly variable U (78–1,598 ppm, mostly <500 ppm) and Th (2,012–11,613 ppm), with Th/U ratios of 2 to 80. The 16 data points plot close to the concordant line and yielded a lower intercept  $^{206}\text{Pb}/^{238}\text{U}$  age of  $145.2 \pm 4.2$  Ma ( $2\sigma$ , MSWD = 4.3; Fig. 12g) on a Tera-Wasserburg plot. After applying the  $^{207}\text{Pb}$ -based correction for common Pb, the weighted mean  $^{206}\text{Pb}/^{238}\text{U}$  age was  $145.3 \pm 3.2$  Ma ( $2\sigma$ , MSWD = 4.1). The common-Pb corrected  $^{208}\text{Pb}/^{232}\text{Th}$  age yielded a weighted mean age of  $144.8 \pm 2.4$  Ma ( $2\sigma$ , MSWD = 4.6; Fig. 12h). When two spots are excluded from the calculation owing to their deviation from the other 14 data, the weighted mean  $^{208}\text{Pb}/^{232}\text{Th}$  age is  $143.5 \pm 1.4$  Ma ( $2\sigma$ , MSWD = 1.5), and the lower intercept and weighted mean  $^{206}\text{Pb}/^{238}\text{U}$  ages change to  $144.3 \pm 4.2$  Ma ( $2\sigma$ , MSWD = 3.8) and  $144.7 \pm 3.2$  Ma ( $2\sigma$ , MSWD = 3.6), respectively.

## Discussion

### *Classification of the low-temperature gold deposits in the Youjiang basin*

Low-temperature sedimentary-hosted gold deposits in the Youjiang basin are generally described as Carlin-type gold deposits because they share characteristics similar to those of Nevada Carlin-type gold deposits (Hu et al., 2002, 2017; Zhang et al., 2003; Su et al., 2009a, 2012; Wang and Groves, 2018). However, a few others have variously proposed them to be Carlin-like (Deng and Wang, 2016), epizonal orogenic (Goldfarb et al., 2019), Carlin-style orogenic (Tran et al., 2016), intermediate between Carlin-type and orogenic (Cline et al., 2013; Su et al., 2018; Xie et al., 2018), and compound of Carlin-type and orogenic gold deposits (Yang et al., 2020).

The prominent examples presented here, such as Jinfeng, Linwang, Jinya, and Nakuang, display structural and strati-

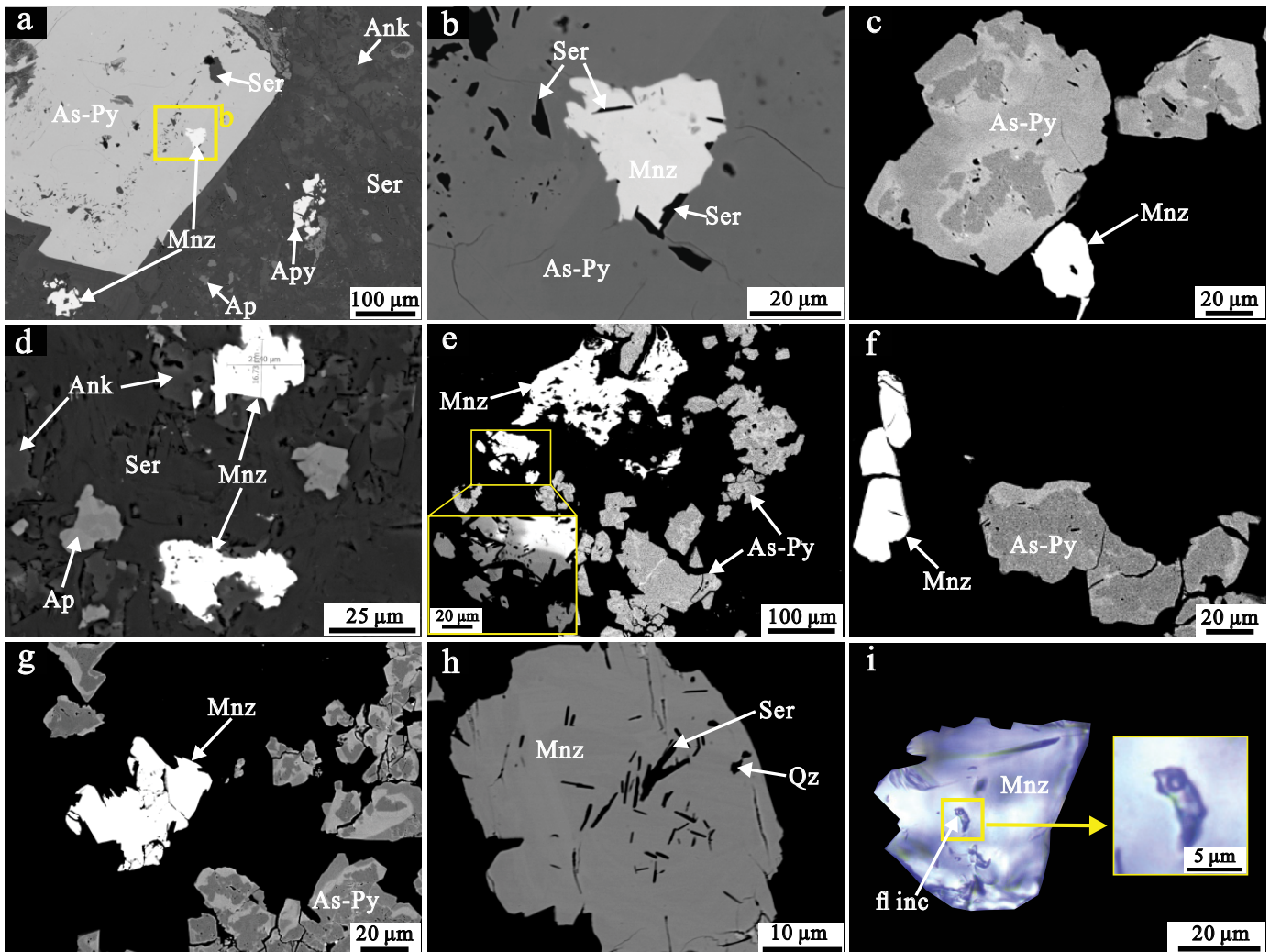


Fig. 14. Photomicrographs in transmitted light and backscattered electron images showing characteristics of hydrothermal monazite in the Badu deposit. (a-c) Monazite associated with arsenian pyrite. (d-g) Monazite distributed in the matrix of ankerite and sericite. (h) Monazite enclosing sericite and quartz. (i) Monazite with primary two-phase fluid inclusions. Abbreviations: Ank = ankerite, Ap = apatite, Apy = arsenopyrite, As-Py = arsenian pyrite, fl inc = fluid inclusion, Mnz = monazite, Qz = quartz, Ser = sericite.

graphic-controlled replacement mineralization of calcareous siltstone host rocks that contain Fe-bearing carbonate minerals. Hydrothermal alterations related to gold mineralization are characterized by dissolution and silicification of carbonate and argillization of silicates. Mineral paragenesis is dominated by ore-stage quartz, carbonate, sericite, or illite, auriferous arsenian pyrite and arsenopyrite that formed by sulfidation, and late ore-stage fracture- or open space-filling stibnite, realgar, quartz, and calcite. Additionally, the ore and ore-stage pyrite are anomalously enriched in Au, S, As, Sb, Hg, and Cu, and gold is predominantly incorporated into arsenian pyrite or arsenopyrite as invisible form of ionically bound  $Au^{+1}$  (Yan, J., et al., 2018; Wu, 2018; Xie et al., 2018; W. Gao, unpub. data, 2020). These features, also shared by the largest Shuiyindong deposit in the basin, are comparable to those of Carlin-type gold deposits in Nevada (Hu et al., 2002, 2017; Su et al., 2009a, 2012, 2018).

The main differences between Carlin-type gold deposits in the Youjiang basin and those in Nevada are the greater abun-

dance of  $CO_2$  in fluid inclusions, introduction of K in sericite, and important but less intense decarbonatization that resulted in Fe-poor dolomite as a stable and prominent mineral during mineralization (Su et al., 2009a; Cline et al., 2013; Xie et al., 2018; this study), which suggest that they formed at higher pressures and depths from less acidic fluids (Su et al., 2018; Xie et al., 2018). However, as pointed out by Wang and Groves (2018), these differences are well within the limits of variation of other coherent gold deposit classes.

The Badu deposit is located close to other sedimentary rock-hosted Carlin-type gold deposits within the basin. The No. II sedimentary-hosted orebody displays highly consistent characteristics with those of above examples such as Jinfeng, Linwang, Jinya, and Nakuang. In most respects the dolerite-hosted orebodies are also similar. Firstly, the least altered dolerites contain numerous Fe-bearing igneous minerals, which is analogous to the Fe-bearing dolomite in the sedimentary-hosted Carlin-type gold deposits. Such reactive Fe-bearing minerals serve as a chemical trap and requirement for

Carlin-type gold mineralization (Stenger et al., 1998; Hofstra and Cline, 2000; Fortuna et al., 2003). Secondly, the mineralized dolerites exhibit hydrothermal alteration, mineral paragenesis, element association, and low base metals and high Au/Ag ratios, which are essentially the same as those in the sedimentary rock-hosted Carlin-type gold deposits. Gold was also primarily incorporated into the lattice of arsenian pyrite as invisible gold. Thirdly, fluid inclusions have similar low homogenization temperatures of 201° to 301°C (with a mode around 245°C) and low salinities (0.02–3.52 wt % NaCl equiv), but have higher CO<sub>2</sub> contents (Dong, 2017).

The dolerite-hosted orebodies of Badu differ in that carbonate dissolution is absent, whereas silicate minerals are ankeritized and sericitized. Igneous Fe-bearing minerals, e.g., clinopyroxene, titanite, and ilmenite, were altered to ankerite, sericite, and rutile. The Fe released by alteration was sulfidized to form gold-bearing arsenian pyrite and arsenopyrite. This process is reminiscent of carbonate dissolution in sedimentary rock-hosted Carlin-type deposits, which also resulted in the release of Fe into ore-forming fluids and precipitation of gold-bearing arsenian pyrite by sulfidation (Hofstra and Cline, 2000; Cline et al., 2005; Su et al., 2009a, 2012). Another difference of the dolerite-hosted orebodies is the occurrence of quartz veins or veinlets, instead of the disseminated jasperoidal quartz and calcite veins in sedimentary rock-hosted Carlin-type gold deposits (Su et al., 2009a, b). Petrographic and geochemical characteristics suggest that the dissolution of silicate minerals and depletion of SiO<sub>2</sub> in dolerite resulted in quartz saturation and precipitation of quartz in fractures during mineralization. This process is analogous to the dissolution of carbonate and release of CaO and CO<sub>2</sub> to form widespread calcite veins in sedimentary rock-hosted Carlin-type gold deposits (Su et al., 2009a, b). Such quartz veins or veinlets are generally associated with gold mineralization and serve as a pathfinder for gold mineralization. Additionally, Badu differs in that K was introduced and Na and Li were removed, which is typical of altered igneous rocks in Nevada Carlin-type gold deposits (Phinisey et al., 1996; Ressel et al., 2000; Yigit and Hofstra, 2003).

Taken together, we therefore conclude that the hydrothermal Au deposits in the Youjiang basin are typical of Carlin-type gold deposits, that Badu is simply a dolerite-hosted equivalent of the other Carlin-type gold deposits within the Youjiang basin, and that the three aforementioned differences may be controlled by the lithology of the host rocks.

#### *Evaluation and interpretation of the zircon U-Th/He data*

As shown in Figure 11a, single grain zircon U-Th/He ages in this study vary from  $161.6 \pm 2.3$  to  $105.0 \pm 1.4$  Ma, except for one grain from Jinya, which yielded age of  $84.1 \pm 1.1$  Ma. The variation is greater than the analytical uncertainty, necessitating evaluation of the factors that contributed the large age range. Previous studies have shown that the following factors can influence U-Th/He ages: He implantation from neighboring U- and Th-bearing minerals, presence of U- and Th-rich mineral inclusions that produce excess <sup>4</sup>He, contribution of <sup>4</sup>He from the decay of <sup>147</sup>Sm, heterogeneous distribution of parent nuclides, difference in grain size, and radiation damage caused by radioactive decay (Farley et al., 1996; Reiners and Farley, 2001; Reiners, 2005; Shuster et al., 2006; Flowers

et al., 2007; Spiegel et al., 2009; Gautheron et al., 2012; Guenther et al., 2013; Danišik et al., 2017).

In this study, the dated zircons have much higher U and Th contents than the surrounding minerals, e.g., sulfides, sericite, quartz, and carbonate minerals. Moreover, there is a strong positive correlation between eU and corrected zircon <sup>4</sup>He content (Fig. 11b). Thus, the effects of He implantation and excess <sup>4</sup>He of U- and Th-bearing mineral inclusions are insignificant. Except for BD-1, the dated samples were from the Middle Triassic strata, which have similar provenance as identified by the age spectra of detrital zircons and geochemical features of host rocks (Yang et al., 2012; Qiu, L., et al., 2017). The probability of zircon with U and Th zoning is random, but the younger U-Th/He ages have a bias toward JY samples. The dispersion of zircon U-Th/He ages, thus, is unlikely to be due to the heterogeneous distribution of U and Th elements.

Radiation damage (eU) has two contrasting effects on U-Th/He ages by impeding and facilitating He diffusion at lower and higher damage, as respectively manifested by positive and negative eU age correlations (Reiners, 2005; Shuster et al., 2006; Guenther et al., 2013; Danišik et al., 2017). As shown in Figure 11d, U-Th/He ages and eU in single sample show positive (e.g., LW-2, BD-1, and JY-1), negative (e.g., LW-3), or no clear (JF-1 and NK) correlations. Zircon grains with lower eU generally yielded much younger U-Th/He ages than other grains from the same sample, e.g., JF-2@1, LW-2@1, and BD-1@2. Additionally, the larger zircon grains tend to yield older ages (Fig. 11c). Among these, JF, LW, and NK samples display a positive correlation between grain size (R<sub>s</sub>) and zircon U-Th/He age. Likewise, JY samples have much younger ages and smaller grain sizes (R<sub>s</sub>).

Thus, we surmise that grain size and radiation damage can account for the scatter of zircon U-Th/He ages. Because of relatively lower eU and/or smaller grain size, the zircons of JY-1, JF-2@1, and LW-2@1 likely had lower U-Th/He block temperatures so that they were more easily affected by late thermal events, which yielded younger U-Th/He ages (Betsi et al., 2012; Danišik et al., 2015; Wolff et al., 2015). In contrast, the larger zircon grains had higher block temperatures of 180° to 200°C. When the aforementioned outliers are excluded, the zircon U-Th/He ages yielded similar weighted mean ages of 146 to 130 Ma.

However, whether the zircon U-Th/He ages recorded the actual timing of a regional thermal event must be carefully evaluated. Firstly, the ages are significantly younger than the ages of the host strata and dolerite, indicating they were related to a postdepositional thermal event that completely, or at least partially, reset the zircon U-Th/He system (Danišik et al., 2015). Secondly, fluid inclusion data suggest that Carlin-type gold deposits in the Youjiang basin formed at temperatures of 230° to 270°C and 200° to 240°C for the early barren and main mineralized stages, respectively (Zhang et al., 2003; Su et al., 2009a; Gu et al., 2012; Dong, 2017), which is higher than the closure temperature of 180° to 200°C for the zircon U-Th/He system (Reiners, 2005). Additionally, the typical life span of hydrothermal systems is generally longer than 0.1 to 1 m.y. (McInnes et al., 2005), and the estimated duration of hydrothermal fluid flow related to Carlin-type mineralization is at least ~25 to 45 k.y. (Hickey et al., 2014), both obviously longer than the time span required for resetting the zircon U-Th/

He system. Thus, in mineralized samples the temperatures and durations of ore-forming fluids related to Carlin-type gold deposits could completely reset the U-Th/He clock of zircon (Arehart et al., 2003). Thirdly, late ore-stage calcite formed at temperatures of less than 125° to 140°C that are much lower than the closure temperature of zircon U-Th/He system (Su et al., 2009a; Gu et al., 2012; Cline, 2018), and no evidence supports more than one fluid event. Finally, samples collected from different deposits, lithology, and depths yielded similar U-Th/He ages—except for Jinya, which yielded much younger U-Th/He ages—indicating they experienced a single heating event followed by rapid cooling. Thus, we infer that the ages are representative of a single thermal event, rather than a cooling event or a mixed age.

The 146 to 130 Ma age range also suggests that there were no subsequent thermal events with temperatures higher than 180° to 200°C. Consequently, the timing of Carlin-type gold deposits must be older than, or equal to, 146 to 130 Ma. This interpretation is consistent with the burial and uplift history of the Youjian basin, which was monotonously uplifted after the Late Triassic (Du et al., 2009; Qiu et al., 2016). Thermal history models suggest that the Middle Triassic strata had burial temperatures of 120° to 150°C 146 to 130 m.y. ago (Qiu et al., 2016), consistent with the lithostatic temperatures calculated based on the formation depth of 4.3 km for Carlin-type gold deposits and a gradient of 30° to 35°C/km (Su et al., 2009a, 2018). Thus, regional heating due to burial was insufficient to reset the zircon U-Th/He system. Rather, the 146 to 130 Ma ages from Carlin-type gold deposits suggest that temperatures higher than 180° to 200°C were localized along structures where there were significant fluxes of hydrothermal fluids. This interpretation is supported by the 150 to 130 Ma Sm-Nd isochron ages of hydrothermal calcite in mineralized samples (Su et al., 2009b; Tan et al., 2019; Zheng et al., 2019).

#### *Hydrothermal origin and interpretation of U-Th-Pb age for monazite*

The monazite grains whose ages were determined in this study are from mineralized dolerite with disseminated gold-bearing pyrite and arsenopyrite. The monazite is spatially associated with gold-bearing pyrite or intergrown with alteration minerals related to gold mineralization. In addition, the monazite contains primary two-phase fluid inclusions, which are similar to those from ore-stage quartz veinlets. Geochemically, the monazite is characterized by relatively low Th contents (mostly <1 wt %), which is less than igneous monazite (3–5 wt %) and characteristic of hydrothermal monazite (Schandl and Gorton, 2004). Thus, we infer that the monazite is hydrothermal in origin and crystallized during gold mineralization.

On the Tera-Wasserburg plot, the monazite grains cluster on the lower intercept, suggesting that low fractions of common Pb were incorporated into monazite. Thus, the effect of common Pb on the age calculation is minor such that the lower intercept age is consistent with the <sup>207</sup>Pb-corrected <sup>206</sup>Pb/<sup>238</sup>U age. However, the high Th/U ratios (2–80) of the monazite grains allow that excess <sup>206</sup>Pb produced by decay of excess <sup>230</sup>Th may have affected the <sup>206</sup>Pb/<sup>238</sup>U ages (Schoene, 2014). Because the actual Th/U ratios of ore-forming fluids are unknown, it is impossible to apply a correction using the equations of Schärer (1984) and Parrish (1990). In such cases,

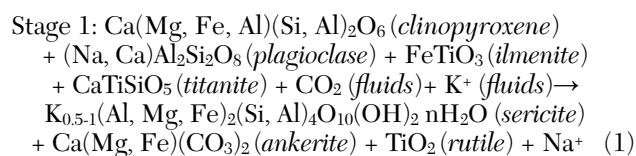
the <sup>206</sup>Pb/<sup>232</sup>Th age is considered to be more robust (Janots et al., 2012; Schulze et al., 2015; Zhou et al., 2019). Moreover, monazites with high Th/U ratios often contain more radiogenic <sup>206</sup>Pb (decayed from <sup>232</sup>Th) than <sup>206</sup>Pb (decayed from <sup>238</sup>U), such that the <sup>206</sup>Pb/<sup>232</sup>Th age of monazite is less sensitive to the common Pb correction (Janots et al., 2012). Compared to the <sup>207</sup>Pb-corrected <sup>206</sup>Pb/<sup>238</sup>U ages, the <sup>206</sup>Pb/<sup>232</sup>Th ages of the monazite grains in this study are more consistent, demonstrating that the weighted mean corrected <sup>206</sup>Pb/<sup>232</sup>Th age of 143.5 ± 1.4 Ma is preferable.

#### *Hydrothermal origin and interpretation of U-Pb age for rutile*

The rutile has many features that indicate it is hydrothermal in origin and genetically related to gold mineralization. Firstly, rutile is absent in fresh dolerite, has only been identified in altered and mineralized dolerite, and is much younger than magmatic zircon. Secondly, the intergrowths of rutile and ankerite mimic the morphologies of ilmenite exsolution in titanite and coarse-grained ilmenite with inclusions of plagioclase and clinopyroxene in unaltered dolerite, respectively. This suggests that rutile essentially formed by the breakdown and pseudomorphic replacement of magmatic ilmenite (Velásquez et al., 2014; Pochon et al., 2017). The high Fe, Cr, and V contents of the rutile are also suggestive of Fe-Ti-bearing precursors (Pereira et al., 2019). Rutile nucleated and grew at the original textural position of ilmenite during hydrothermal fluid-rock reactions, partially preserving the crystallographic orientation (Rabbia et al., 2009). Experimental study has shown that the ilmenite is replaced by rutile via pseudomorphic interface-coupled dissolution-reprecipitation (Janssen et al., 2010). Thirdly, rutile displays compositional zoning and enrichments of W, Fe, V, Cr, and Nd elements that are characteristic of hydrothermal rutile associated with various types of gold mineralization (Urban et al., 1992; Rice et al., 1998; Clark and Williams-Jones, 2004; Scott, 2005; Scott and Radford, 2007; Scott et al., 2011; Doyle et al., 2015; Agangi et al., 2019). Hydrothermal rutile associated with mesothermal gold deposits invariably has high W and Sb contents and Sb/V ratios (Clark and Williams-Jones, 2004; Agangi et al., 2019).

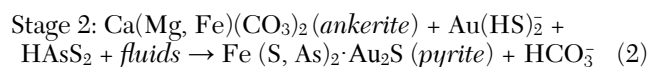
Importantly, petrographic characteristics show that the rutile has consistent spatial and textural associations with ankerite, sericite, and gold-bearing iron sulfides. The microtextures in Figure 13 indicate that alteration occurred in three steps:

1. At the incipient stage of alteration, primary plagioclase, clinopyroxene, titanite, and ilmenite were altered and replaced by hydrothermal fluids with high CO<sub>2</sub> and K<sup>+</sup> contents, resulting in the formation of ankerite, sericite, and rutile according to reaction (1).



2. Then, pyrite crystallized and grew at the expense of ankerite as shown in reaction (2), to form the inclusion-rich pyrite cores.





This reaction also resulted in the formation of open spaces due to the different densities of ankerite and pyrite (Velásquez et al., 2014).

- Continued saturation with FeS<sub>2</sub> enabled pyrite to crystallize in open spaces to form the inclusion-free rims. The net effect of these reactions was sulfidation of ankerite and precipitation of gold-bearing arsenian pyrite. Gold, together with other elements, was incorporated into the pyrite structure. Given that the pyrite core and rim contain invisible gold and have similar sulfur isotope compositions (W. Gao, unpub. data, 2020), we infer that the two generations of pyrite were penecontemporaneous and formed from an evolving episode of fluid flow.

Thus, we suggest that the formation of hydrothermal rutile is intimately associated with gold mineralization and texturally synchronous with or slightly earlier than gold-bearing pyrite. Its U-Pb age is therefore representative of the timing of gold formation. The rutile dated in this study is characterized by compositional zoning, low U contents, and appreciable common Pb compositions, which result in an imprecise age. However, data from different zones with various contents of U, Th, W, and Fe have variable amounts of radiogenic versus common Pb, producing a regression line with  $f_{206}$  ranging from 4.1 to 88.1% on the Tera-Wasserburg concordia diagrams. The regression line, therefore, defines a robust lower intercept age of  $141.7 \pm 5.8$  Ma ( $2\sigma$ , MSWD = 1.04).

Interpretation of rutile U-Pb age depends on the closure temperature of Pb diffusion. Grain size, core-rim structure, and cooling rate of rutile have a great influence on its U-Pb closure temperature. Consequently, rutile Pb-blocking temperatures of 370° to 500°C (Mezger et al., 1989; Li et al., 2003, 2013a) and 490° to 630°C (Cherniak, 2000; Vry and Baker, 2006; Kooijman et al., 2010) have been reported. The rutile dated in this study is 50 to 200 μm in length, indicating a Pb closure temperature of ~500°C (Li et al., 2013a). Fluid inclusion data suggest the ore-forming temperature of the Badu deposit was about 201° to 301°C (Dong, 2017), which is much lower than the estimated rutile U-Pb closure temperature. Additionally, zircon U-Th/He dating suggests that there were not any significant thermal or hydrothermal events with temperatures above 180° to 220°C since 146 to 130 Ma in the Youjiang basin. Thus, post-ore Pb diffusion in rutile was unlikely, as supported by the well-preserved compositional zoning. Thus, hydrothermal rutile could start its U-Pb clock and remain closed as soon as it formed. That means the age of  $141.7 \pm 5.8$  Ma ( $2\sigma$ , MSWD = 1.04) could represent the timing of gold mineralization.

#### *Implications for the age and geodynamic setting of Carlin-type gold deposits in the Youjiang basin*

To frame this study, we compiled information on the ages of ore deposits in South China (Fig. 15). At Badu, the host dolerite yielded a zircon U-Pb age of  $212.2 \pm 1.9$  Ma ( $2\sigma$ , MSWD = 0.55), which provides an upper limit on the age of gold mineralization. Zircon U-Th/He dates from Badu and four other Carlin-type gold deposits yielded similar weighted mean ages of 146 to 130 Ma, which place a minimum constraint on gold

mineralization. Hydrothermal rutile and monazite directly associated with gold mineralization yielded U-Th-Pb ages of  $141.7 \pm 5.8$  Ma ( $2\sigma$ , MSWD = 1.04) and  $143.5 \pm 1.4$  Ma ( $2\sigma$ , MSWD = 1.5), respectively. Together (Fig. 15c), these age determinations suggest that Badu and the other Carlin-type gold deposits were produced by an Early Cretaceous hydrothermal event in the Youjiang basin, which is reinforced by the hydrothermal apatite age of the Nibao deposit (Chen et al., 2019). This examination of sustainability of hydrothermal rutile and monazite U-Th-Pb chronometers might inspire other works to accurately determine mineralization ages of hydrothermal gold deposits worldwide.

These ages coincide with those of a pulse of magmatism and hydrothermal ore deposits in the Nanling Range W-Sn metallogenic belt in South China, which is one of the world's largest W-Sn provinces (Fig. 15a; Hu and Zhou, 2012). Although previous researchers have shown that 160 to 150 Ma was the most important period of W-Sn mineralization in the Nanling Range (Yuan et al., 2008, 2011; Hu and Zhou, 2012; Hu et al., 2012; Mao, J.W., et al., 2013; Zhang et al., 2015, 2017), another important period of mineralization at 147 to 135 Ma was also present in this belt (Mao et al., 2004; Zhang et al., 2006; Zeng et al., 2009; Fu et al., 2011; Qi et al., 2012; Li et al., 2018; Xiong et al., 2020). Ages of 148 to 135 Ma were also obtained on W-Sn mineralization in the Southeastern Coastal W-Sn metallogenic belt (Liu et al., 2017, 2018; Qiu, Z.W., et al., 2017; Yan, Q.H., et al., 2018) and in the Middle-Lower Yangtze River porphyry Cu belt (Mao et al., 2011; Mao, Z.H., et al., 2013; Pan et al., 2017). All of the above-mentioned mineralization ages were reliably and precisely constrained by cassiterite U-Pb, molybdenite Re-Os, and muscovite Ar-Ar dating (Fig. 15b). Thus, we infer that they are all related to an Early Cretaceous geodynamic setting (Hu et al., 2017).

Based on a synthesis of structural, petrological, geochronological, and geochemical data it is now clear that South China experienced a tectonic transition from contraction to large-scale extension at ca. 148 to 135 Ma in response to rollback of the subducted Paleo-Pacific plate beneath South China (Hu and Zhou, 2012; Li et al., 2014; Dong et al., 2015). The evidence presented herein suggests that the Early Cretaceous Carlin-type gold mineralization in the Youjiang basin was a direct consequence of this dynamic setting, which is analogous to that of Eocene Carlin-type gold deposits in Nevada (Cline et al., 2005; Ressel and Henry, 2006; Muntean et al., 2011). Another episode of gold mineralization in the Youjiang basin has potentially been revealed by hydrothermal rutile U-Pb of  $213.6 \pm 5.4$  Ma at the medium-sized Zhesang deposit in the southern margin of the basin (Pi et al., 2017), which temporally coincides with mafic magmatism in Badu and Funing districts (Pi et al., 2016; this study), indicating a postcollisional extension setting. However, mineralization characteristics and scale of this gold mineralization event need further study.

## Conclusions

The genesis and geodynamic setting of Carlin-type gold deposits in the Youjiang basin have been contentious because of the uncertain age of mineralization. The Badu disseminated gold deposit, with as much as 70% of the ore hosted in dolerite that is unaffected by diagenesis and older hydrothermal

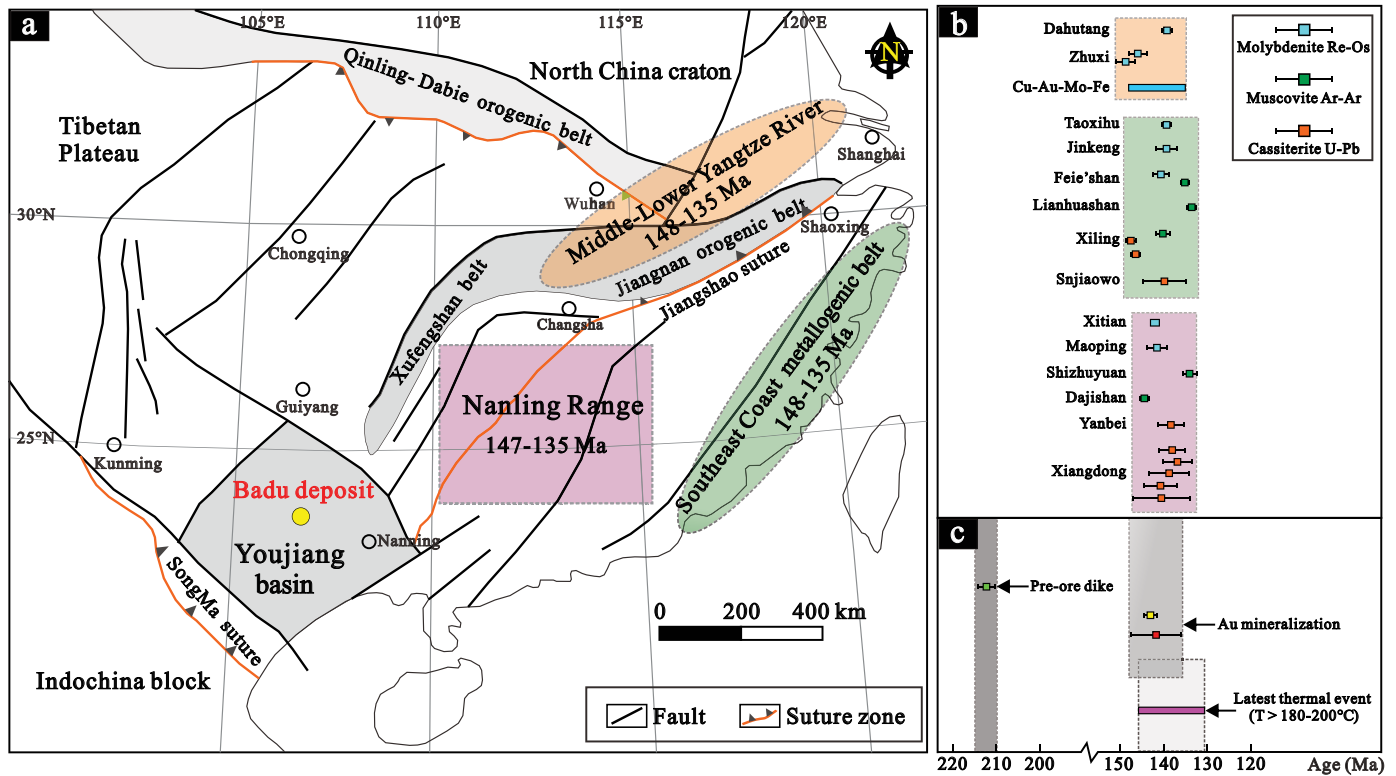


Fig. 15. (a) Simplified geologic map of the South China block showing the structural framework and locations of the Youjiang basin, Nanling Range, Southeast Coast, and Middle-Lower Yangtze River W-Sn metallogenic belt (modified from Hu et al., 2017). (b) Summary of Early Cretaceous mineralization ages of ore deposits in the Nanling Range, Southeast Coast, and Middle-Lower Yangtze River W-Sn metallogenic belt, which were reliably and precisely constrained by cassiterite U-Pb, molybdenite Re-Os, and muscovite Ar-Ar dating. The mineralization age data are from numerous literature sources (Mao et al., 2004; Zhang et al., 2006; Zeng et al., 2009; Mao et al., 2011; Mao, Z.H., et al., 2013; Pan et al., 2017; Qiu, Z.W., et al., 2017; Liu et al., 2017, 2018; Li et al., 2018; Yan, Q.H., et al., 2018; Xiong et al., 2020). (c) Mineralization ages for the Badu deposit (this study).

events, provides a unique opportunity for geochronologic study that is absent in most Carlin-type gold deposits.

1. Geologic, mineralogical, and geochemical investigations suggest that Badu has alteration types, mineral paragenesis, element associations, and residence of gold similar to those of sedimentary rock-hosted Carlin-type gold deposits in the basin.
2. In situ SIMS U-Pb dating on magmatic zircon from the least altered dolerite yielded a robust emplacement age of  $212.2 \pm 1.9$  Ma ( $2\sigma$ , MSWD = 0.55), providing a maximum constraint on the age of gold mineralization. Zircon U-Th/He dating, conducted on Badu and four other representative sedimentary rock-hosted Carlin-type gold deposits in the Youjiang basin, yielded nearly consistent mean U-Th/He ages of 146 to 130 Ma, which place a lower limit on, or reveal the actual age of, gold mineralization.
3. At Badu, hydrothermal rutile and monazite, closely associated with ore-stage ankerite, sericite, and gold-bearing pyrite, were identified in mineralized dolerite. In situ SIMS U-Th-Pb dating on rutile and monazite yielded robust ages of  $141.7 \pm 5.8$  Ma ( $2\sigma$ , MSWD = 1.04) and  $143.5 \pm 1.4$  Ma ( $2\sigma$ , MSWD = 1.5), respectively, which are comparable to hydrothermal apatite Th-Pb age of  $141 \pm 3$  Ma from Chen et al. (2019) and represent the age of gold mineralization.

4. Carlin-type gold mineralization in the Youjiang basin might have formed during the transition from contraction to extension of South China resulting from slab rollback, which is analogous to Carlin-type gold deposit in the western United States.

### Acknowledgments

This research was financially supported by the National Natural Science Foundation of China (41830432, U1812402) and the National 973 Program of China (2014CB440906). We would like to thank Prof. Jiafei Xiao for his help during field work. We are grateful to Prof. Peter W. Reiners for helping with zircon U-Th/He analyses, to Mr. Yu Liu, Ms. Xiaoxiao Ling, and Ms. Jiao Li for helping with SIMS zircon, rutile, and monazite U-Th-Pb isotope analyses, to Mr. Peijun Lin and Zengsheng Li for helping with EPMA analyses, and to Ms. Hongxia Ma for her laborious preparation of sample mounts. We thank Prof. David Groves, Prof. Ines Pereira, and an anonymous reviewer for their constructive reviews, which have greatly improved the quality of the manuscript.

### REFERENCES

- Agangi, A., Reddy, S.M., Plavsa, D., Fougereuse, D., Clark, C., Roberts, M., and Johnson, T.E., 2019, Antimony in rutile as a pathfinder for orogenic gold deposits: *Ore Geology Reviews*, v. 106, p. 1–11.


- Arehart, G.B., Foland, K.A., Naeser, C.W., and Kesler, S.E., 1993,  $^{40}\text{Ar}/^{39}\text{Ar}$ , K/Ar, and fission track geochronology of sediment-hosted disseminated gold deposits at Post-Betze, Carlin trend, northeastern Nevada: *Economic Geology*, v. 88, p. 622–646.
- Arehart, G.B., Chakurian, A.M., Tretbar, D.R., Christensen, J.N., McInnes, B.R., and Donelick, R.A., 2003, Evaluation of radioisotope dating of Carlin-type deposits in the Great Basin, western North America, and implications for deposit genesis: *Economic Geology*, v. 98, p. 235–248.
- Ayers, J.C., and Watson, E.B., 1993, Rutile solubility and mobility in super-critical aqueous fluids: *Contributions to Mineralogy and Petrology*, v. 114, p. 321–330.
- Betsi, T.B., Lentz, D., McInnes, B., and Evans, N.J., 2012, Emplacement ages and exhumation rates for intrusion-hosted Cu-Mo-Sb-Au mineral systems at Freegold Mountain (Yukon, Canada): Assessment from U-Pb, Ar-Ar, and (U-Th)/He geochronometers: *Canadian Journal of Earth Sciences*, v. 49, p. 653–670.
- Brandon, M.T., Roden-Tice, M.K., and Garver, J.I., 1998, Late Cenozoic exhumation of the Cascadia accretionary wedge in the Olympic Mountains, northwest Washington State: *Geological Society of America Bulletin*, v. 110, p. 985–1009.
- Bureau of Geology and Mineral Resources of GuangXi Province (BGM-RGX), 1992, Magmatic rocks in the Baduxu district: 1:50000 regional geological survey report for Baduxu district (G-48-140-B): Guilin, the People's Republic of China, p. 119–143.
- Cai, J.X., and Zhang, K.J., 2009, A new model for the Indochina and South China collision during the late Permian to the Middle Triassic: *Tectonophysics*, v. 467, p. 35–43.
- Chakurian, A.M., Arehart, G.B., Donelick, R.A., Zhang, X., and Reiners, P.W., 2003, Timing constraints of gold mineralization along the Carlin trend utilizing apatite fission-track,  $^{40}\text{Ar}/^{39}\text{Ar}$ , and apatite (U-Th)/He methods: *Economic Geology*, v. 98, p. 1159–1171.
- Chen, M.H., Mao, J.W., Uttley, P.J., Norman, T., Wu, L.L., Zheng, J.M., and Qin, Y.Z., 2007, Structure analysis and structural metallogenesis of Jinfeng gold deposit in Guizhou Province: *Mineral Deposits*, v. 26, p. 380–396 (in Chinese with English abs.).
- Chen, M.H., Huang, Q.W., Hu, Y., Chen, Z.Y., and Zhang, W., 2009a, Genetic types of phyllosilicate (micas) and its  $^{39}\text{Ar}/^{40}\text{Ar}$  dating in Lannigou gold deposit, Guizhou Province, China: *Acta Mineralogica Sinica*, v. 29, p. 353–362 (in Chinese with English abs.).
- Chen, M.H., Zhang, W., Yang, Z.X., Lu, G., Hou, K.J., and Liu, J.H., 2009b, Zircon SHRIMP U-Pb age and Hf isotopic composition of Baiceng ultrabasic dykes in Zhenfeng County, southwestern Guizhou Province: *Mineral Deposits*, v. 28, p. 240–250 (in Chinese with English abs.).
- Chen, M.H., Huang, Q.W., Li, J.X., Jiang, B.C., and Zhang, C.M., 2010, Structure analysis and structural metallogenies of the Linwang gold deposit, Leye, Guangxi, China: *Geotectonica et Metallogenia*, v. 34, p. 349–361 (in Chinese with English abs.).
- Chen, M.H., Mao, J.W., Bierlein, F.P., Norman, T., and Uttley, P.J., 2011, Structural features and metallogenesis of the Carlin-type Jinfeng (Lannigou) gold deposit, Guizhou Province, China: *Ore Geology Reviews*, v. 43, p. 217–234.
- Chen, M.H., Lu, G., and Li, X.H., 2012, Muscovite  $^{40}\text{Ar}/^{39}\text{Ar}$  dating of the quartz porphyry veins from northwest Guangxi, China, and its geological significance: *Geological Journal of China Universities*, v. 18, p. 106–116 (in Chinese with English abs.).
- Chen, M.H., Zhang, Y., Meng, Y.Y., Lu, G., and Liu, S.Q., 2014, The confirmation of the upper limit of metallogenetic epoch of Liaotun gold deposit in western Guangxi, China, and its implication on chronology of Carlin-type gold deposits in Yunnan-Guizhou-Guangxi “golden triangle” area: *Mineral Deposits*, v. 33, p. 1–13 (in Chinese with English abs.).
- Chen, M.H., Mao, J.W., Li, C., Zhang, Z.Q., and Dang, Y., 2015, Re-Os isochron ages for arsenopyrite from Carlin-like gold deposits in the Yunnan-Guizhou-Guangxi “golden triangle,” southwestern China: *Ore Geology Reviews*, v. 64, p. 316–327.
- Chen, M.H., Bagas, L., Liao, X., Zhang, Z.Q., and Li, Q.L., 2019, Hydrothermal apatite SIMS Th-Pb dating, constraints on the timing of low-temperature hydrothermal Au deposit in Nibao, SW China: *Lithos*, v. 324–325, p. 418–428.
- Cheng, Y.B., Mao, J.W., Xie, G.Q., Chen, M.H., and Yang, Z.X., 2009, Zircon U-Pb dating of granite in Gejiu super-large tin polymetallic orefield and its significance: *Mineral Deposits*, v. 28, p. 297–312 (in Chinese with English abs.).
- Cheng, Y.B., Mao, J.W., Chen, X.L., and Li, W., 2010, LA-ICP-MS zircon U-Pb dating of the Bozhushan granite in southeastern Yunnan Province and its significance: *Journal of Jilin University (Earth Science Edition)*, v. 40, p. 869–878 (in Chinese with English abs.).
- Cherniak, D.J., 2000, Pb diffusion in rutile: *Contributions to Mineralogy and Petrology*, v. 139, p. 198–207.
- China Geological Survey, 2015, Discovery of large gold deposits in the Jinya deposit, Guangxi: *Gold Science and Technology*, v. 23, p. 54 (in Chinese with English abs.).
- Clark, J.R., and Williams-Jones, A.E., 2004, Rutile as a potential indicator mineral for metamorphosed metallic ore deposits: Montréal, Canada, McGill University, Rapport Final de DIVEX, Sous-projet SC2, p. 1–17.
- Cline, J.S., 2018, Nevada's Carlin-type gold deposits: What we've learned during the past 10 to 15 years: *Reviews in Economic Geology*, v. 20, p. 7–37.
- Cline, J.S., Hofstra, A.H., Muntean, J.L., Tosdal, R.M., and Hickey, K.A., 2005, Carlin-type gold deposits in Nevada: Critical geologic characteristics and viable models: *Economic Geology 100<sup>th</sup> Anniversary Volume*, p. 451–484.
- Cline, J.S., Muntean, J.L., Gu, X.X., and Xia, Y., 2013, A comparison of Carlin-type gold deposits: Guizhou Province, golden triangle, Southwest China, and northern Nevada, USA: *Earth Science Frontiers*, v. 20, p. 1–18.
- Danišik, M., Fodor, L., Dunkl, I., Gerdes, A., Csizmeg, J., Hámor-Vidó, M., and Evans, N.J., 2015, A multi-system geochronology in the Ad-3 borehole, Pannonian basin (Hungary) with implications for dating volcanic rocks by low-temperature thermochronology and for interpretation of (U-Th)/He data: *Terra Nova*, v. 27, p. 258–269.
- Danišik, M., McInnes, B.I.A., Kirkland, C.L., McDonald, B.J., Evans, N.J., and Becker, T., 2017, Seeing is believing: Visualization of He distribution in zircon and implications for thermal history reconstruction on single crystals: *Science Advance*, v. 3, p. e1601121.
- Deng, J., and Wang, Q.F., 2016, Gold mineralization in China: Metallogenic provinces, deposit types and tectonic framework: *Gondwana Research*, v. 36, p. 219–274.
- Dong, S.W., Zhang, Y.Q., Zhang, F.Q., Cui, J.J., Chen, X.H., Zhang, S.H., Miao, L.C., Li, J.H., Shi, W., Li, Z.H., Huang, S.Q., and Li, H.L., 2015, Late Jurassic-Early Cretaceous continental convergence and intracontinental orogenesis in East Asia: A synthesis of the Yanshan Revolution: *Journal of Asian Earth Science*, v. 114, p. 750–770.
- Dong, W.D., 2017, Geochemistry of dolerite-hosted gold deposit along the southern margin of Youjiang basin: Unpublished Ph.D. dissertation, Guiyang, China, Institute of Geochemistry, Chinese Academy of Sciences, 215 p. (in Chinese with English abs.).
- Doyle, M.G., Fletcher, I.R., Foster, J., Large, R.R., Mathur, R., McNaughton, N.J., Meffre, S., Muhling, J.R., Phillips, D., and Rasmussen, B., 2015, Geochronological constraints on the Tropicana gold deposit and Albany-Fraser orogen, Western Australia: *Economic Geology*, v. 110, p. 355–386.
- Du, Y.S., Huang, H.W., Huang, Z.Q., Xu, Y.J., Yang, J.H., and Huang, H., 2009, Basin translation from late Paleozoic to Triassic of Youjiang basin and its tectonic significance: *Geological Science and Technology Information*, v. 28, p. 10–15 (in Chinese with English abs.).
- Du, Y.S., Huang, H., Yang, J.H., Huang, H.W., Tao, P., Huang, Z.Q., Hu, L.S., and Xie, C.X., 2013, The basin translation from late Paleozoic to Triassic of the Youjiang basin and its tectonic significance: *Geological Review*, v. 59, p. 1–11 (in Chinese with English abs.).
- Emsbo, P., Hofstra, A.H., Lauha, E.A., Griffin, G.L., and Hutchinson, R.W., 2003, Origin of high-grade gold ore, source of ore fluid components, and genesis of the Meikle and neighboring Carlin-type deposits, northern Carlin trend, Nevada: *Economic Geology*, v. 98, p. 1069–1105.
- Fan, W.M., Zhang, C.H., Wang, Y.J., Guo, F., and Peng, T.P., 2008, Geochronology and geochemistry of Permian basalts in western Guangxi Province, Southwest China: Evidence for plume-lithosphere interaction: *Lithos*, v. 102, p. 218–236.
- Farley, K.A., Wolf, R.A., and Fallick, A.E., 1996, The effects of long alpha-stopping distances on (U-Th)/He ages: *Geochimica et Cosmochimica Acta*, v. 60, p. 4223–4229.
- Feng, J.R., Mao, J.W., Pei, R.F., Zhou, Z.H., and Yang, Z.X., 2010, SHRIMP zircon U-Pb dating and geochemical characteristics of Laojunshan granite intrusion from the Wazha tungsten deposit, Yunnan Province and their implications for petrogenesis: *Acta Petrologica Sinica*, v. 26, p. 845–857 (in Chinese with English abs.).
- Fielding, I.O.H., Johnson, S.P., Zi, J.W., Rasmussen, B., Muhling, J.R., Dunkley, D.J., Sheppard, S., Wingate, M.T.D., and Rogers, J.R., 2017, Using in situ SHRIMP U-Pb monazite and xenotime geochronology to determine

- the age of orogenic gold mineralization: An example from the Paulsens mine, southern Pilbara craton: *Economic Geology*, v. 112, p. 1205–1230.
- Flowers, R.M., Shuster, D.L., Wernicke, B.P., and Farley, K.A., 2007, Radiation damage control on apatite (U-Th)/He dates from the Grand Canyon region, Colorado Plateau: *Geology*, v. 35, p. 447–450.
- Fortuna, J., Kesler, S.E., and Stenger, D.P., 2003, Source of iron for sulfidation and gold deposition, Twin Creeks Carlin-type deposit, Nevada: *Economic Geology*, v. 98, p. 1213–1224.
- Fu, J.M., Xu, D.M., Yang, X.J., Ma, L.Y., Cai, M.H., Liu, Y.H., Wei, J.Q., Liu, G.Q., Wei, D.F., Chen, X.Q., Cheng, S.B., and Mei, Y.P., 2011, Tin deposits in Nanling Range, in Wang, F.L., and Zhang, X.H., eds., *Research progress of significant tin deposits and related granites in Nanling Range*: Beijing, China University of Geosciences Press, p. 33–35 (in Chinese).
- Gan, C.S., Wang, Y.J., Zhang, Y.Z., Liu, H.C., and Zhang, L.M., 2016, The identification and implications of the Late Jurassic shoshonitic high-Mg andesite from the Youjiang basin: *Acta Petrologica Sinica*, v. 32, p. 3281–3294 (in Chinese with English abs.).
- Gao, W., 2018, Geochronology and geodynamics of Carlin-type gold deposit in the Youjiang basin (NW Guangxi): Unpublished Ph.D. dissertation, Guiyang, China, Institute of Geochemistry, Chinese Academy of Sciences, 169 p. (in Chinese with English abs.).
- Gautheron, C., Tassan-Got, L., Ketcham, R.A., and Donson, K.A., 2012, Accounting for long alpha-particle stopping distances in (U-Th-Sm)/He geochronology: 3D modeling of diffusion, zoning, implantation, and abrasion: *Geochimica et Cosmochimica Acta*, v. 96, p. 44–56.
- Goldfarb, R., Qiu, K.F., Deng, J., Chen, Y.J., and Yang, L.Q., 2019, Orogenic gold deposits of China: Society of Economic Geologists, Special Publication 22, p. 263–324.
- Grant, J.A., 1986, The isocon diagram: a simple solution to Gresens' equation for metasomatic alteration: *Economic Geology*, v. 81, p. 1976–1982.
- Gu, X.X., Zhang, Y.M., Li, B.H., Dong, S.Y., Xue, C.J., and Fu, S.H., 2012, Hydrocarbon and ore-bearing basinal fluids: A possible link between gold mineralization and hydrocarbon accumulation in the Youjiang basin, South China: *Mineralium Deposita*, v. 47, p. 663–682.
- Guenther, W.R., Reiners, P.W., Ketcham, R.A., Nasdala, L., and Giester, G., 2013, Helium diffusion in natural zircon: Radiation damage, anisotropy and the interpretation of zircon (U-Th)/He thermochronology: *American Journal of Science*, v. 313, p. 145–198.
- Hickey, K.A., Baker, S.L.L., Dipple, G.M., Arehart, G.B., and Donelick, R.A., 2014, The brevity of hydrothermal fluid flow revealed by thermal halos around giant gold deposits: Implications for Carlin-type gold systems: *Economic Geology*, v. 109, p. 1461–1487.
- Hofstra, A.H., and Cline, J.S., 2000, Characteristics and models for Carlin-type gold deposits: *Economic Geology*, v. 13, p. 163–220.
- Hofstra, A.H., Snee, L.W., Rye, R.O., Folger, H.W., Phinisey, J.D., Loranger, R.J., Dahl, A.R., Naeser, C.W., Stein, H.J., and Lewchuk, M.T., 1999, Age constraints on Jerritt Canyon and other Carlin-type gold deposits in the western United States: Relationship to mid-Tertiary extension and magmatism: *Economic Geology*, v. 94, p. 769–802.
- Hu, R.Z., and Zhou, M.F., 2012, Multiple Mesozoic mineralization events in South China—an introduction to the thematic issue: *Mineralium Deposita*, v. 47, p. 579–588.
- Hu, R.Z., Su, W.C., Bi, X.W., Tu, G.Z., and Hofstra, A.H., 2002, Geology and geochemistry of Carlin-type gold deposits in China: *Mineralium Deposita*, v. 37, p. 378–392.
- Hu, R.Z., Wei, W.F., Bi, X.W., Peng, J.T., Qi, Y.Q., Wu, L.Y., and Chen, Y.W., 2012, Molybdenite Re-Os and muscovite  $^{40}\text{Ar}/^{39}\text{Ar}$  dating of the Xihuashan tungsten deposit, central Nanling district, South China: *Lithos*, v. 150, p. 111–118.
- Hu, R.Z., Fu, S.L., Huang, Y., Zhou, M.F., Fu, S.H., Zhao, C.H., Wang, Y.J., Bi, X.W., and Xiao, J.F., 2017, The giant South China Mesozoic low-temperature metallogenic domain: Reviews and a new geodynamic model: *Journal of Asian Earth Sciences*, v. 137, p. 9–34.
- Janots, E., Berger, A., Gnos, E., Whitehouse, M., Lewin, E., and Pettke, T., 2012, Constraints on fluid evolution during metamorphism from U-Th-Pb systematics in Alpine hydrothermal monazite: *Chemical Geology*, v. 326–327, p. 61–71.
- Janssen, A., Putnis, A., Geisler, T., and Putnis, C.V., 2010, The experimental replacement of ilmenite by rutile in HCl solutions: *Mineralogical Magazine*, v. 74, p. 633–644.
- Jiang, W., Xiang, Z.J., Xia, W.J., Xia, L., Zhang, H., Phan, V.T., Yan, Q.R., and Wei, W., 2017, Are the mafic intrusive rocks in the Funing area, southeast Yunnan (Southwest China), really derived from the Emeishan plume: New evidence from geological surveys of the Dongbo and Guichao sheets (1:50,000): *Acta Petrologica Sinica*, v. 33, p. 3109–3122 (in Chinese with English abs.).
- Jin, X.Y., 2017, *Geology, mineralization and genesis of the Nibao, Shuiyindong and Yata gold deposit in SW Guizhou province, China*: Ph.D. dissertation, Wuhan, China, China University of Geosciences, 208 p. (in Chinese with English abs.).
- Kesler, S.E., Riciputi, L.C., and Ye, Z.J., 2005, Evidence for a magmatic origin for Carlin-type gold deposits: Isotopic composition of sulfur in the Betze-Post-Screamer deposit, Nevada, USA: *Mineralium Deposita*, v. 40, p. 127–136.
- Ketcham, R.A., Donelick, R.A., and Carlson, W.D., 1999, Variability of apatite fission-track annealing kinetics: III. Extrapolation to geological time scales: *American Mineralogist*, v. 84, p. 1235–1255.
- Kooijman, E., Mezger, K., and Berndt, J., 2010, Constraints on the U-Pb systematics of metamorphic rutile from in situ LA-ICP-MS analysis: *Earth and Planetary Science Letters*, v. 293, p. 321–330.
- Li, J.H., Zhang, Y.Q., Dong, S.W., and Johnston, S.T., 2014, Cretaceous tectonic evolution of South China: A preliminary synthesis: *Earth-Science Reviews*, v. 134, p. 98–136.
- Li, Q., Zhao, K.D., Lai, P.C., Jiang, S.Y., and Chen, W., 2018, Petrogenesis of Cretaceous volcanic-intrusive complex from the giant Yanbei tin deposit, South China: Implication for multiple magma sources, tin mineralization, and geodynamic setting: *Lithos*, v. 296–299, p. 163–180.
- Li, Q.L., Li, S.G., Zheng, Y.F., Li, H.M., Massonne, H.J., and Wang, Q.C., 2003, A high precision U-Pb age of metamorphic rutile in coesite-bearing eclogite from the Dabie Mountains in central China: A new constraint on the cooling history: *Chemical Geology*, v. 200, p. 255–265.
- Li, Q.L., Lin, W., Su, W., Li, X.H., Shi, Y.H., Liu, Y., and Tang, G.Q., 2011, SIMS U-Pb rutile age of low-temperature eclogites from southwestern Chinese Tianshan, NW China: *Lithos*, v. 122, p. 76–86.
- Li, Q.L., Yang, Y.N., Shi, Y.H., and Lin, W., 2013a, Eclogite rutile U-Pb dating: Constraint for formation and evolution of continental collisional orogen: *Chinese Sciences Bulletin*, v. 58, p. 2279–2284.
- Li, Q.L., Li, X.H., Lan, Z.W., Guo, C.L., Yang, Y.N., Liu, Y., and Tang, G.Q., 2013b, Monazite and xenotime U-Th-Pb geochronology by ion microprobe: Dating highly fractionated granites at Xihuashan tungsten mine, SE China: Contributions to Mineralogy and Petrology, p. 65–80.
- Li, X.H., Liu, Y., Li, Q.L., Guo, C.H., and Chamberlain, K.R., 2009, Precise determination of Phanerozoic zircon Pb/Pb age by multi-collector SIMS without external standardization: *Geochemistry Geophysics Geosystems*, v. 10, p. Q04010.
- Li, Z.X., and Li, X.H., 2007, Formation of the 1300-km-wide intracontinental orogen and postorogenic magmatic province in Mesozoic South China: A flat-slab subduction model: *Geology*, v. 35, p. 179–182.
- Liu, P., Mao, J.W., Pirajno, F., Jia, L.H., Zhang, F., and Li, Y., 2017, Ore genesis and geodynamic setting of the Lianhuashan porphyry tungsten deposit, eastern Guangdong Province, SE China: Constraints from muscovite  $^{40}\text{Ar}/^{39}\text{Ar}$  and zircon U-Pb dating and Hf isotopes: *Mineralium Deposita*, v. 5, p. 1–18.
- Liu, P., Mao, J.W., Santosh, M., Xu, L.G., Zhang, R.Q., and Jia, L.H., 2018, The Xiling Sn deposit, eastern Guangdong Province, southeast China: A new genetic model from  $^{40}\text{Ar}/^{39}\text{Ar}$  muscovite and U-Pb cassiterite and zircon geochronology: *Economic Geology*, v. 113, p. 511–530.
- Liu, S., Su, W.C., Hu, R.Z., Feng, C.X., Gao, S., Coulson, I.M., Wang, T., Feng, G.Y., Tao, Y., and Xia, Y., 2010, Geochronological and geochemical constraints on the petrogenesis of alkaline ultramafic dykes from southwest Guizhou Province, SW China: *Lithos*, v. 114, p. 253–264.
- Liu, Y.P., Li, Z.X., Li, H.M., Guo, L.G., Xu, W., Ye, L., Li, C.Y., and Pi, D.H., 2007, U-Pb geochronology of cassiterite and zircon from the Dulong Sn-Zn deposit: Evidence for Cretaceous large-scale granitic magmatism and mineralization events in southeastern Yunnan province, China: *Acta Petrologica Sinica*, v. 23, p. 967–976 (in Chinese with English abs.).
- Mao, J.W., Xie, G.Q., Li, X.F., Zhang, C.Q., and Mei, Y.X., 2004, Mesozoic large scale mineralization and multiple lithospheric extensions from South China: *Earth Science Frontiers*, v. 11, p. 45–55 (in Chinese with English abs.).
- Mao, J.W., Xie, G.Q., Duan, C., Pirajno, F., Ishiyama, D., and Chen, Y.C., 2011, A tectonogenetic model for porphyry-skarn-strata bound Cu-Au-Mo-Fe and magnetite-apatite deposits along the Middle-Lower Yangtze River valley, eastern China: *Ore Geology Reviews*, v. 43, p. 294–314.
- Mao, J.W., Cheng, Y.B., Chen, M.H., and Pirajno, F., 2013, Major types and time-space distribution of Mesozoic ore deposits in South China and their geodynamic settings: *Mineralium Deposita*, v. 48, p. 267–294.

- Mao, Z.H., Cheng, Y.B., Liu, J.J., Yuan, S.D., Wu, S.H., Xiang, X.K., and Luo, X.H., 2013, Geology and molybdenite Re-Os age of the Dahutang granite related veinlets-disseminated tungsten ore field in the Jiangxi Province, China: *Ore Geology Reviews*, v. 53, p. 422–433.
- McInnes, B.I.A., Evans, N.J., Fu, F.Q., and Garwin, S., 2005, Application of thermochronology to hydrothermal ore deposits: *Reviews in Mineralogy and Geochemistry*, v. 58, p. 467–498.
- Meinhold, G., 2010, Rutile and its applications in earth sciences: *Earth-Science Reviews*, v. 102, p. 1–28.
- Mezger, K., Hanson, G.N., and Bohlen, S.R., 1989, High-precision U-Pb ages of metamorphic rutiles: Application to the cooling history of high-grade terranes: *Earth and Planetary Science Letters*, v. 96, p. 106–118.
- Muntean, J.L., and Cline, J.S., 2018, Diversity of Carlin-type gold deposits: *Reviews in Economic Geology*, v. 20, p. 1–5.
- Muntean, J.L., Cline, J.S., Simon, A.C., and Longo, A.A., 2011, Magmatic-hydrothermal origin of Nevada's Carlin-type gold deposits: *Nature Geoscience*, v. 4, p. 122–127.
- Palenik, C.S., Utsunomiya, S., Reich, M., Kesler, S.E., Wang, L.M., and Ewing, R.C., 2004, "Invisible" gold revealed: Direct imaging of gold nanoparticles in a Carlin-type deposit: *American Mineralogist*, v. 89, p. 1359–1366.
- Pan, X.F., Hou, Z.Q., Li, Y., Chen, G.H., Zhao, M., Zhang, T.F., Zhang, C., Wei, J., and Kang, C., 2017, Dating the giant Zhuxi W-Cu deposit (Taqian-Fuchun ore belt) in South China using molybdenite Re-Os and muscovite Ar-Ar system: *Ore Geology Reviews*, v. 86, p. 719–733.
- Parrish, R.R., 1990, U-Pb dating of monazite and its application to geological problems: *Canadian Journal of Earth Sciences*, v. 27, p. 1431–1450.
- Pereira, L., Storey, C., Darling, J., Lana, C., and Alkmin, A.R., 2019, Two billion years of evolution enclosed in hydrothermal rutile: Recycling of the São Francisco craton crust and constraints on gold remobilization processes: *Gondwana Research*, v. 68, p. 69–92.
- Phinisey, J.D., Hofstra, A.H., Snee, L.W., Roberts, T.T., Dahl, A.R., and Loranger, R.J., 1996, Evidence for multiple episodes of igneous and hydrothermal activity and constraints on the timing of gold mineralization, Jerritt Canyon district, Elko County, Nevada: *Geological Society of Nevada, Geology and Ore Deposits of the American Cordillera Symposium*, Reno-Sparks, Nevada, April 1995, Proceedings, p. 15–39.
- Pi, Q.H., Hu, R.Z., Bi, X.W., Peng, K.Q., Wu, J.B., Wei, Z.W., and Huang, Y., 2016, Geochronology of the Zhesang gold deposit and mafic rock in Funing County of Yunnan Province, with special reference to the dynamic background of Carlin-type gold deposits in the Dian-Qian-Gui region: *Acta Petrologica Sinica*, v. 32, p. 3331–3342 (in Chinese with English abs.).
- Pi, Q.H., Hu, R.Z., Xiong, B., Li, Q.L., and Zhong, R.C., 2017, In situ SIMS U-Pb dating of hydrothermal rutile, reliable age for the Zhesang Carlin-type gold deposit in the golden triangle region, SW China: *Mineralium Deposita*, v. 52, p. 1179–1190.
- Pochon, A., Beaudoin, G., Branquet, Y., Boulvais, P., Gloaguen, E., and Gapais, D., 2017, Metal mobility during hydrothermal breakdown of Fe-Ti oxides: Insights from Sb-Au mineralizing event (Variscan Armorican Massif, France): *Ore Geology Reviews*, v. 91, p. 66–90.
- Qi, H.W., Hu, R.Z., Wang, X.F., Qu, W.J., Bi, X.W., and Peng, J.T., 2012, Molybdenite Re-Os and muscovite  $^{40}\text{Ar}/^{39}\text{Ar}$  dating of quartz vein-type W-Sn polymetallic deposits in Northern Guangdong, South China: *Mineralium Deposita*, v. 47, p. 607–622.
- Qiu, L., Yan, D.P., Tang, S.L., Wang, Q., Yang, W.X., Tang, X.L., and Wang, J.B., 2016, Mesozoic geology of southwestern China: Indosinian foreland overthrusting and subsequent deformation: *Journal of Asian Earth Sciences*, v. 122, p. 91–105.
- Qiu, L., Yan, D.P., Yang, W.X., Wang, J.B., Tang, X.L., and Ariser, S., 2017, Early to Middle Triassic sedimentary records in the Youjiang basin, South China: Implications for Indosinian orogenesis: *Journal of Asian Earth Sciences*, v. 141, p. 125–139.
- Qiu, Z.W., Yan, Q.H., Li, S.S., Wang, H., Tong, L.X., Zhang, R.Q., Wei, X.P., Li, P., Wang, L.M., Bu, A., and Yan, L.M., 2017, Highly fractionated Early Cretaceous I-type granites and related Sn polymetallic mineralization in the Jinkeng deposit, eastern Guangdong, SE China: Constraints from geochronology, geochemistry, and Hf isotopes: *Ore Geology Reviews*, v. 88, p. 718–738.
- Rabbia, O.M., Hernandez, L.B., French, D.H., King, R.W., and Ayers, J.C., 2009, The El Teniente porphyry Cu-Mo deposit from a hydrothermal rutile perspective: *Mineralium Deposita*, v. 44, p. 849–866.
- Rasmussen, B., Sheppard, S., and Fletcher, I.R., 2006, Testing ore deposit models using in situ U-Pb geochronology of hydrothermal monazite, Paleoproterozoic gold mineralization in northern Australia: *Geology*, v. 34, p. 77–80.
- Reich, M., Kesler, S.E., Utsunomiya, S., Palenik, C.S., Chrissyoulis, S.L., and Ewing, R.C., 2005, Solubility of gold in arsenian pyrite: *Geochimica et Cosmochimica Acta*, v. 69, p. 2781–2796.
- Reiners, P.W., 2005, Zircon (U-Th)/He thermochronometry: *Reviews in Mineralogy and Geochemistry*, v. 58, p. 151–179.
- Reiners, P.W., and Farley, K.A., 2001, Influence of crystal size on apatite (U-Th)/He thermochronology: An example from the Bighorn Mountains, Wyoming: *Earth and Planetary Science Letters*, v. 188, p. 413–420.
- Reiners, P.W., Spell, T.L., Nicolescu, S., and Zanetti, K.A., 2004, Zircon (U-Th)/He thermochronometry: He diffusion and comparisons with  $^{40}\text{Ar}/^{39}\text{Ar}$  dating: *Geochimica et Cosmochimica Acta*, v. 68, p. 1857–1887.
- Ressel, M.W., and Henry, C.D., 2006, Igneous geology of the Carlin trend, Nevada, Development of the Eocene plutonic complex and significance for Carlin-type gold deposits: *Economic Geology*, v. 101, p. 347–383.
- Ressel, M.W., Noble, D.C., Henry, C.D., and Trudel, W.S., 2000, Dike-hosted ores of the Beast deposit and the importance of Eocene magmatism in gold mineralization of the Carlin trend, Nevada: *Economic Geology*, v. 95, p. 1417–1444.
- Rice, C., Darke, K., and Still, J., 1998, Tungsten-bearing rutile from the Kori Kollo gold mine Bolivia: *Mineralogical Magazine*, v. 62, p. 421–429.
- Sarma, D.S., McNaughton, N.J., Fletcher, I.R., Groves, D.I., Ram Mohan, M., and Balaram, V., 2008, Timing of gold mineralization in the Hutti gold deposit, Dharwar craton, South India: *Economic Geology*, v. 103, p. 1715–1727.
- Sarma, D.S., Fletcher, I.R., Rasmussen, B., McNaughton, N.J., Ram Mohan, M., and Groves, D.I., 2011, Archaean gold mineralization synchronous with late orotization of the western Dharwar craton, India: 2.52 Ga U-Pb ages of hydrothermal monazite and xenotime in gold deposits: *Mineralium Deposita*, v. 46, p. 273–288.
- Schandl, E.S., and Gorton, M.P., 2004, A textural and geochemical guide to the identification of hydrothermal monazite: Criteria for selection of samples for dating epigenetic hydrothermal ore deposits: *Economic Geology*, v. 99, p. 1027–1035.
- Schärer, U., 1984, The effect of initial  $^{230}\text{Th}$  disequilibrium on young U-Pb ages: The Makalu case, Himalaya: *Earth and Planet Science Letters*, v. 67, p. 191–204.
- Schoene, B., 2014, U-Th-Pb geochronology, in Holland, H., and Turekian, K., eds., *Treatise on geochemistry*, 2nd ed.: Amsterdam, Elsevier, p. 341–378.
- Schulze, D.J., Davis, D.W., Helmstaedt, H., and Joy, B., 2015, Timing of the Cenozoic "Great Hydration" event beneath the Colorado Plateau: Th-Pb dating of monazite in Navajo volcanic field metamorphic eclogite xenoliths: *Geology*, v. 43, p. 727–730.
- Scott, K.M., 2005, Rutile geochemistry as a guide to porphyry Cu-Au mineralization, Northparkes, New South Wales, Australia: *Geochemistry: Exploration, Environment, Analysis*, v. 5, p. 247–253.
- Scott, K.M., and Radford, N.W., 2007, Rutile compositions at the Big Bell Au deposit as a guide for exploration: *Geochemistry: Exploration, Environment, Analysis*, v. 7, p. 353–361.
- Scott, K.M., Radford, N.W., Hough, R.M., and Reddy, S.M., 2011, Rutile compositions in the Kalgoorlie Goldfields and their implications for exploration: *Australian Journal of Earth Sciences*, v. 58, p. 803–812.
- Shuster, D.L., Flowers, R.M., and Farley, K.A., 2006, The influence of natural radiation damage on helium diffusion kinetics in apatite: *Earth and Planetary Science Letters*, v. 249, p. 148–161.
- Simon, G., Kesler S.E., and Chrissyoulis, S., 1999, Geochemistry and texture of gold-bearing arsenian pyrite, Twin Creeks, Nevada; implications for deposition of gold in Carlin-type deposit: *Economic Geology*, v. 94, p. 405–421.
- Song, C.A., Feng, Z.H., and Lei, L.Q., 2009, Geotectonic metallogenic evolution and belt of tin polymetal ore and exploration in Guangxi: *Journal of Guilin University of Technology*, v. 29, p. 207–215 (in Chinese with English abs.).
- Spiegel, C., Kohn, B., Belton, D., Berner, Z., and Gleadow, A., 2009, Apatite (U-Th-Sm)/He thermo-chronology of rapidly cooled samples: The effect of He implantation: *Earth and Planetary Science Letters*, v. 285, p. 105–114.
- Stenger, D.P., Kesler, S.E., Peltonen, D.R., and Tapper, C.J., 1998, Deposition of gold in Carlin-type deposits; the role of sulfidation and decarbonation at Twin Creeks, Nevada: *Economic Geology*, v. 93, p. 201–215.
- Su, W.C., Xia, B., Zhang, H.T., Zhang, X.C., and Hu, R.Z., 2008, Visible gold in arsenian pyrite at the Shuiyidong Carlin-type gold deposit, Guizhou,

- China: Implications for the environment and processes of ore formation: *Ore Geology Reviews*, v. 33, p. 667–679.
- Su, W.C., Heinrich, C.A., Pettke, T., Zhang, X.C., Hu, R.Z., and Xia, B., 2009a, Sediment-hosted gold deposits in Guizhou, China: Products of wall-rock sulfidation by deep crustal fluids: *Economic Geology*, v. 104, p. 73–93.
- Su, W.C., Hu, R.Z., Xia, B., Xia, Y., and Liu, Y.P., 2009b, Calcite Sm-Nd isochron age of the Shuiyindong Carlin-type gold deposit, Guizhou, China: *Chemical Geology*, v. 258, p. 269–274.
- Su, W.C., Zhang, H.T., Hu, R.Z., Ge, X., Xia, B., Chen, Y.Y., and Zhu, C., 2012, Mineralogy and geochemistry of gold-bearing arsenian pyrite from the Shuiyindong Carlin-type gold deposit, Guizhou, China: Implications for gold depositional processes: *Mineralium Deposita*, v. 47, p. 653–662.
- Su, W.C., Dong, W.D., Zhang, X.C., Shen, N.P., Hu, R.Z., Hofstra, A.H., Cheng, L.Z., Xia, Y., and Yang, K.Y., 2018, Carlin-type gold deposits in the Dian-Qian-Gui “golden triangle” of Southwest China: *Reviews in Economic Geology*, v. 20, p. 157–185.
- Suo, S.T., Bi, X.M., Zhao, W.X., and Hou, G.J., 1998, Very low-grade metamorphism and its geodynamical significance of Triassic strata within the Youjiang River basin: *Scientia Geologica Sinica*, v. 33, p. 396–405 (in Chinese with English abs.).
- Tan, Q.P., Xia, Y., Xie, Z.J., Wang, Z.P., Wei, D.T., Zhao, Y.M., Yan, J., and Li, S.T., 2019, Two hydrothermal events at the Shuiyindong Carlin-type gold deposit in southwestern China: Insight from Sm-Nd dating of fluorite and calcite: *Minerals*, v. 9, article 230.
- Tompsett, G.A., Bownmaker, G.A., Cooney, R.P., Metson, J.B., Rodgers, K.A., and Seakins, J.M., 1995, The Raman spectrum of brookite, TiO<sub>2</sub> (Pbca, Z = 8): *Journal of Raman Spectroscopy*, v. 26, p. 57–62.
- Tran, T.H., Nevolko, P.A., Ngo, T.P., Svetlitskaya, T.V., Vu, H.L., Redin, Y., Tran, T.A., Pham, T.D., and Ngo, T.H., 2016, Geology, geochemistry and sulphur isotopes of the Hat Han gold-antimony deposit, NE Vietnam: *Ore Geology Reviews*, v. 78, p. 69–84.
- Tretbar, D., Arehart, G.B., and Christensen, J.N., 2000, Dating gold deposition in a Carlin-type gold deposit using Rb/Sr methods on the mineral galkhaite: *Geology*, v. 28, p. 947–950.
- Urban, A.J., Hoskins, B.F., and Grey, I.E., 1992, Characterization of V-Sb-W-bearing rutile from the Hemlo gold deposit, Ontario: *The Canadian Mineralogist*, v. 30, p. 319–326.
- Velásquez, G., Béziat, D., Salvi, S., Siebenaller, L., Borisova, A.Y., Pokrovski, G., and Parseval, P., 2014, Formation and deformation of pyrite and implications for gold mineralization in the El Callao district, Venezuela: *Economic Geology*, v. 109, p. 457–486.
- Vielreicher, N.M., Groves, D.I., Snee, L.W., Fletcher, I.R., and McNaughton, N.J., 2010, Broad synchronicity of three gold mineralization styles in the Kalgoolie gold field: SHRIMP, U-Pb, and <sup>40</sup>Ar/<sup>39</sup>Ar geochronological evidence: *Economic Geology*, v. 105, p. 187–227.
- Vielreicher, N.M., Groves, D.I., McNaughton, N.J., and Fletcher, I.R., 2015, The timing of gold mineralization across the eastern Yilgarn craton using U-Pb geochronology of hydrothermal phosphate minerals: *Mineralium Deposita*, v. 50, p. 391–428.
- Vry, J.K., and Baker, J.A., 2006, LA-MC-ICP-MS Pb-Pb dating of rutile from slowly cooled granulites: Confirmation of the high closure temperature for Pb diffusion in rutile: *Geochimica et Cosmochimica Acta*, v. 70, p. 1807–1820.
- Wang, Q.F., and Groves, D., 2018, Carlin-style gold deposits, Youjiang basin, China: Tectono-thermal and structural analogues of the Carlin-type gold deposits, Nevada, USA: *Mineralium Deposita*, v. 53, p. 909–918.
- Wang, Y.J., Fan, W.M., Zhang, G.W., and Zhang, Y.H., 2013, Phanerozoic tectonics of the South China block: Key observations and controversies: *Gondwana Research*, v. 23, p. 1273–1305.
- Wang, Z.P., 2013, Origin and geodynamic setting of the low-temperature deposits in southwestern Guizhou, China: Examples of gold and antimony deposit: Unpublished Ph.D. dissertation, Guiyang, China, Institute of Geochemistry, Chinese Academy of Sciences, 150 p. (in Chinese with English abs.).
- Wolff, R., Dunkl, I., Kempe, U., and von Eynatten, H., 2015, The age of the latest thermal overprint of tin and polymetallic deposits in the Erzgebirge, Germany: Constraints from fluorite (U-Th-Sm)/He thermochronology: *Economic Geology*, v. 110, p. 2025–2040.
- Wu, W., 2018, Mineralization of the Jinya and Nakuang Carlin-like gold deposits in Northwest Guangxi: Published M.S. dissertation, Beijing, China, China University of Geosciences, 69 p. (in Chinese with English abs.).
- Xie, Z.J., Xia, Y., Cline, J.S., Koenig, A., Wei, D.T., Tan, Q.P., and Wang, Z.P., 2018, Are there Carlin-type gold deposits in China? A comparison of the Guizhou, China, deposits with Nevada, USA, deposits: *Reviews in Economic Geology*, v. 20, p. 187–233.
- Xiong, Y.Q., Shao, Y.J., Cheng, Y.B., and Jiang, S.Y., 2020, Discrete Jurassic and Cretaceous mineralization events at the Xiangdong W(-Sn) deposit, Nanling Range, South China: *Economic Geology*, v. 115, p. 385–413.
- Yan, D.P., Zhou, M.F., Wang, Y.C., and Xia, B., 2006, Structural and geochronological constraints on the tectonic evolution of the Dulong-Song Chay tectonic dome in Yunnan Province, SW China: *Journal of Asian Earth Sciences*, v. 28, p. 332–353.
- Yan, J., Hu, R.Z., Liu, S., Lin, Y.T., Zhang, J.C., and Fu, S.L., 2018, Nano-SIMS element mapping and sulfur isotope analysis of Au-bearing pyrite from Lannigou Carlin-type Au deposit in SW China: New insights into the origin and evolution of Au-bearing fluids: *Ore Geology Reviews*, v. 92, p. 29–41.
- Yan, Q.H., Wang, H., Qiu, Z.W., Wei, X.P., Li, P., Dong, R., Zhang, X.Y., and Zhou, K.L., 2018, Origin of Early Cretaceous A-type granite and related Sn mineralization in the Sanjiaowo deposit, eastern Guangdong, SE China and its tectonic implication: *Ore Geology Reviews*, v. 93, p. 60–80.
- Yang, J.H., Cawood, P.A., Du, Y.S., Huang, H., and Hu, L.S., 2012, Detrital record of Indosinian mountain building in SW China: Provenance of the Middle Triassic turbidites in the Youjiang basin: *Tectonophysics*, v. 574–575, p. 105–117.
- Yang, L., Deng, J., Groves, D.I., Wang, Q.F., Zhang, L., Wu, W., Qin, K., and Zhang, Q.Z., 2020, Recognition of two contrasting structural- and mineralogical-gold mineral systems in the Youjiang basin, China-Vietnam: Orogenic gold in the south and Carlin-type in the north: *Geoscience Frontiers*, v. 111, p. 1477–1494.
- Yang, W.X., Yan, D.P., Qiu, L., Chen, F., Mu, H.X., and Wang, X.W., 2018, The Mesozoic-Cenozoic deformation sequences of the Badu Complex anticline and their significance for the evolution of the Nanpanjiang basin: *Earth Science Frontiers*, v. 25, p. 033–046 (in Chinese with English abs.).
- Yigit, O., and Hofstra, A.H., 2003, Litho-geochemistry of Carlin-type gold mineralization in the Gold Bar district, Battle Mountain-Eureka trend, Nevada: *Ore Geology Reviews*, v. 22, p. 201–224.
- Yuan, S.D., Peng, J.T., Hu, R.Z., Li, H.M., Shen, N.P., and Zhang, D.L., 2008, A precise U-Pb age on cassiterite from the Xianghualing tin-polymetallic deposit (Hunan, South China): *Mineralium Deposita*, v. 43, p. 375–382.
- Yuan, S.D., Peng, J.T., Hao, S., Li, H.M., Geng, J.Z., and Zhang, D.L., 2011, In situ LA-MC-ICP-MS and ID-TIMS U-Pb geochronology of cassiterite in the giant Furong tin deposit, Hunan Province, South China: New constraints on the timing of tin-polymetallic mineralization: *Ore Geology Reviews*, v. 43, p. 235–242.
- Zeng, Z.L., Zhang, Y.Z., Zhu, X.P., Chen, Z.H., Wang, C.H., and Wu, W.J., 2009, Re-Os isotopic dating of molybdenite from the Maoping tungsten-tin deposit in Chongyi county of southern Jiangxi Province and its geological significance: *Rock and Mineral Analysis*, v. 28, p. 209–214 (in Chinese with English abs.).
- Zhang, R.Q., Lu, J.J., Wang, R.C., Yang, P., Zhu, J.C., Yao, Y., Gao, J.F., Li, C., Lei, Z.H., Zhang, W.L., and Guo, W.M., 2015, Constraints of in situ zircon and cassiterite U-Pb, molybdenite Re-Os and muscovite <sup>40</sup>Ar-<sup>39</sup>Ar ages on multiple generations of granitic magmatism and related W-Sn mineralization in the Wangxianling area, Nanling Range, South China: *Ore Geology Reviews*, v. 65, p. 1021–1042.
- Zhang, R.Q., Lu, J.J., Lehmann, B., Li, C.Y., Li, G.L., Zhang, L.P., Guo, J., and Sun, W.D., 2017, Combined zircon and cassiterite U-Pb dating of the Piaotang granite-related tungsten-tin deposit, southern Jiangxi tungsten district, China: *Ore Geology Reviews*, v. 82, p. 268–284.
- Zhang, W.L., Hua, R.M., Wang, R.C., Chen, P.R., and Li, H.M., 2006, New dating of the Dajishan granite and related tungsten mineralization in southern Jiangxi: *Acta Geologica Sinica*, v. 80, p. 956–962 (in Chinese with English abs.).
- Zhang, X.C., Spiro, B., Halls, C., Stanley, C.J., and Yang, K.Y., 2003, Sediment-hosted disseminated gold deposits in Southwest Guizhou, PRC: Their geological setting and origin in relation to mineralogical, fluid inclusion, and stable-isotope characteristics: *International Geology Reviews*, v. 45, p. 407–470.
- Zhao, J.H., Zhou, M.F., Yan, D.P., Zheng, J.P., and Li, J.W., 2011, Reappraisal of the ages of Neoproterozoic strata in South China: No connection with the Grenvillian orogeny: *Geology*, v. 39, p. 299–302.
- Zheng, L.L., Yang, R.D., Gao, J.B., Chen, J., Liu, J.Z., and Li, D.P., 2019, Quartz Rb-Sr isochron ages of two type orebodies from the Nibao Carlin-type gold deposit, Guizhou, China: *Minerals*, v. 9, p. 399–413.
- Zhou, M.F., Zhao, J.H., and Qi, L., 2006, Zircon U-Pb geochronology and elemental and Sr-Nd isotopic geochemistry of Permian mafic rocks in the

- Funing area, SW China: *Contributions to Mineralogy and Petrology*, v. 151, p. 1–19.
- Zhou, H.Y., Sun, X.M., Wu, Z.W., and Huang, Q., 2019, Timing of skarn gold deposition in the giant Beiya polymetallic gold deposit, Southwest China: Constraints from in situ monazite SIMS U-Th-Pb geochronology: *Ore Geology Reviews*, v. 106, p. 226–237.
- Zhu, J.J., Hu, R.Z., Richards, J.P., Bi, X.W., Stern, R., and Lu, G., 2017, No genetic link between Late Cretaceous felsic dikes and Carlin-type Au deposits in the Youjiang basin, Southwest China: *Ore Geology Reviews*, v. 84, p. 328–337.



**Wei Gao** is currently a postdoctoral researcher at the Institute of Geochemistry, Chinese Academy of Sciences. He finished his B.S. degree in geology in 2009 from Sun Yat-Sen University, and then received his Ph.D. degree in economic geology from the Institute of Geochemistry, Chinese Academy of Sciences, in 2019. His research interests focus on the geochronology, ore-forming process, and remobilization upgrade of Carlin-type gold deposits in the Youjiang basin, China, using a combination of field mapping, mineralogy, element and isotope geochemistry, and geochronology.

